Short Papers

Quasi-TEM Characteristic Impedance of Micromachined CMOS Coplanar Waveguides

Mehmet Ozgur, Veljko Milanović, Christian Zincke, Michael Gaitan, and Mona E. Zaghloul

***Abstract*—Micromachined coplanar waveguides (CPW's) fabricated in CMOS technology consist of glass-encapsulated metal conductor strips, fully suspended by selective etching of the silicon substrate. The minimum amount of etching necessary for proper operation of the micromachined waveguides is determined by using an isolation criterion. In this paper, the quasi-TEM characteristic impedance of a CPW is derived, including the finite conductor thickness and the thicknesses of surrounding dielectric layers. The employed analytical approach is based on conformal mapping and the partial capacitance technique. The losses both in conductor and dielectric layers are neglected. The analytical results and proposed approximations are verified by integral-equation computation and by measurement of various sample structures.**

***Index Terms*—Microelectromechanical devices, micromachining, transmission-line theory.**

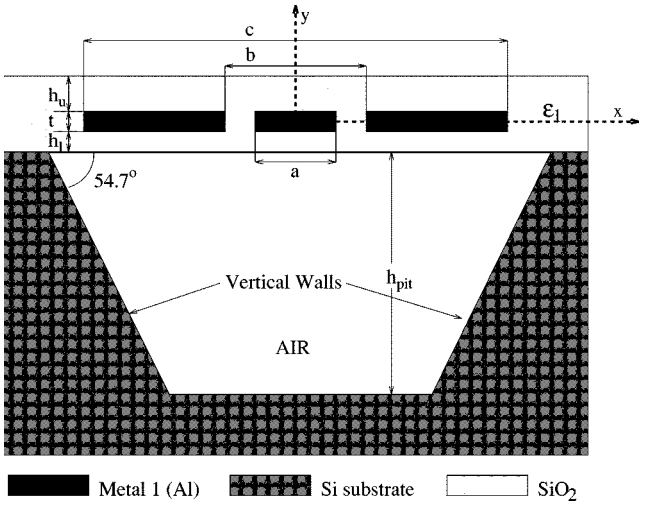

Fig. 1. Cross-sectional view of a fully suspended CPW.

I. Introduction

Micromachining is one of the important emerging technologies that offers high functionality and performance at the system level for a lower cost. Integration and packaging of micromachined components have been receiving great attention [1]. Among many micromachined components, waveguides are especially important for high-frequency applications. Recently, implementation of efficient microwave coplanar waveguides (CPW's) has been demonstrated in CMOS technology by selective etching of silicon substrate [2]. Schematic cross section of such a CPW is illustrated in Fig. 1.

Accurate characterization of micromachined CMOS CPW's can be performed by using numerical techniques. However, in many cases, it is desirable to have fast, compact, and accurate analytic formulas, which can be integrated into computer-aided design (CAD) environments. However, closed-form analytic expressions are very difficult to get for realistic cases. Here, we introduce two simplifications to achieve closed-form expressions. First, we assume the quasi-TEM mode propagation. As long as the materials are lossless and the cross-sectional dimensions are much shorter than operating wavelength, this assumption is valid. It has been shown that, for micromachined CPW's, this is good up to millimeter-wave frequencies [3]. As a result, propagation characteristics can be expressed in terms of quasi-static capacitances that are calculated by using the conformal mapping technique [4], [5]. Second, we assume that by micromachining, the electromagnetic fields are well isolated from lossy substrate. We introduce a criterion for sufficient substrate isolation in order to be able to neglect the effect of remaining silicon substrate.

Manuscript received January 21, 1999. This work was supported in part by the Space and Naval Warfare Systems Center. The work of M. Ozgur and V. Milanović was supported by RF Microsystems.

M. Ozgur, V. Milanović, C. Zincke, and M. E. Zaghloul are with the Department of Electrical Engineering and Computer Science, George Washington University, Washington, DC 20052 USA (e-mail: ozgur@seas.gwu.edu).

M. Gaitan is with Semiconductor Electronics Division, National Institute of Standards and Technology, Gaithersburg, MD 20899-8124 USA.

Publisher Item Identifier S 0018-9480(00)03767-4.

In the presence of a substrate, usually signal-to-ground strip spacings are significantly larger than strip thickness; therefore, the results of the conformal mapping with zero-thickness strips have been acceptable for CPW's with thick substrate. Difficulty arises once the CPW is micromachined. In order to keep the impedance the same, the signal-to-ground strip spacing is decreased. For a standard 50-Ω micromachined CPW fabricated on CMOS, this distance becomes such that one should consider both thickness of dielectric films and the conductor thickness. On the other hand, the conformal mapping techniques developed to calculate quasi-static CPW capacitances assume either zero conductor thickness with finite thickness dielectric layers [6]–[9] or semiinfinite dielectric layers with finite conductor thickness [3]. Therefore, the extension of conformal mapping techniques to handle the micromachined CPW's is necessary. Hence, we propose a novel method to characterize a lossless CPW, with a finite thickness conductor and finite thickness dielectric layers.

II. Analytical Approach

Consider the micromachined symmetric CPW illustrated in Fig. 1. If we assume a quasi-TEM mode propagation and neglect the effect of the remaining substrate, the propagation properties, i.e., the characteristic impedance and effective permittivity, can be expressed in terms of the following two capacitances:

$$Z_0 = \frac{1}{c\sqrt{C_{\text{air}}C_{\text{total}}}} \quad \epsilon_{\text{eff}} = \frac{C_{\text{total}}}{C_{\text{air}}} \tag{1}$$

where C_{total} is the quasi-static capacitance per unit length between the signal strip and two ground strips, C_{air} is the equivalent air–line capacitance per unit length obtained by removing all dielectrics. As a result of this assumption, the problem is reduced to the computation of two capacitances. First, however, we introduce the criterion for sufficient isolation, which allows us to neglect the effect of the substrate in subsequent calculations.

A. Criterion for Sufficient Substrate Isolation of a Fully-Suspended CMOS CPW

The total capacitance, $C_{\rm total}$, depends on the geometry of the etched pit, as can be seen in Fig. 1. Since it is very difficult to deal with the silicon boundary by using conformal mapping methods, it is desirable to neglect it entirely. In order to do this consistently over different cases, we introduce the lower half-plane capacitance $C_{\rm hp}$, which is the sum of contributions from the thin oxide layer, air gap, and remaining silicon substrate. To simplify its calculation, we neglect the contribution by the $\langle 111\rangle$ silicon crystal walls (sidewalls). $C_{\rm hp}$ can then be expressed as a function of air–gap height $h_{\rm pit}$

$$C_{\rm hp}(h_{\rm pit}) = C(h_l,\, \epsilon_1 - 1) + C(h_l + h_{\rm pit},\, 1 - \epsilon_{\rm Si}) + C(\infty,\, \epsilon_{\rm Si}) \tag{2}$$

where the function $C(h,\, \epsilon)$ gives the capacitance per unit length between the signal and ground conductors contributed by only dielectric layer with the dielectric constant ϵ and the thickness h. It is calculated as

$$C(h,\, \epsilon) = 2\epsilon_0\epsilon\,\frac{K(k_h')}{K(k_h)}, \qquad \text{with } k_h = \frac{c_h}{b_h}\sqrt{\frac{b_h^2 - a_h^2}{c_h^2 - a_h^2}} \tag{3}$$

where $K(k)$ is the complete elliptic integral of the first kind, k is the argument of the integral, and k' is related to k by $k' = \sqrt{(1-k^2)}$. Here, x_h is

$$x_h = \sinh\,\frac{\pi x}{2h}, \qquad \text{for } x = a,\, b,\, c. \tag{4}$$

Since $C_{\rm hp}(h_{\rm pit})$ is monolithically decreasing with $h_{\rm pit}$, there exists a minimum $h_{\rm pit,\,min}$ for which

$$\frac{C_{\rm hp}(h_{\rm pit,\,min}) - C_{\rm hp}(\infty)}{C_{\rm hp}(\infty)} = 0.01 \tag{5}$$

is satisfied. If the actual pit depth is greater than or equal to $h_{\rm pit,\,min}$, the error in the computation when the remaining substrate is entirely neglected, will be less than or equal to 1%.

For the CPW structures used in this study, $h_{\rm pit,\,min}$ values are calculated using the definition given here. For the first CPW in Table I, $h_{\rm pit,\,min} = 83\ \mu$m, and for the last two CPW's, $h_{\rm pit,\,min} = 190\ \mu$m. These etching values can be achieved by careful design and post processing of CPW's.

Having defined and calculated the sufficient isolation criterion, in the remainder of this paper, we will assume that $h_{\rm pit} \geq h_{\rm pit,\,min}$ for all structures and ignore the remaining substrate.

B. Capacitance of a Finite Thickness CPW in Air

Air capacitance of CPW is defined as the capacitance when the dielectric constant is set as $\epsilon_1 = 1$. The conductor boundary in the RQ-plane [see Fig. 2(a)], which is the upper right quadrant of the general CPW structure in Fig. 1 represented in the complex domain, is then mapped into the real axis in the ZQ-plane [see Fig. 2(b)] by using the Schwartz–Christoffel mapping

$$r = \int_{z_0}^{z} \frac{dr}{dz}\,dz, \qquad \text{with } \frac{dr}{dz} = \sqrt{\frac{(z^2 - z_1^2)}{(z^2 - z_2^2)}} \tag{6}$$

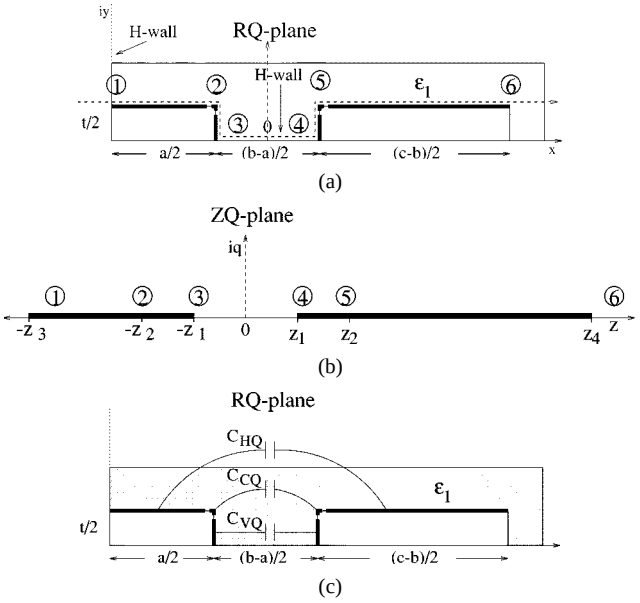

Fig. 2. (a) First quadrant of the CPW structure is shown with the transformation axis (dashed). (b) After the transformation described in (6), the transformation axis is mapped onto z-axis. (c) Capacitance contributions due to horizontal and vertical walls and corners of the CPW.

where r is a point in the RQ-plane and z is the corresponding point in the ZQ-plane. The transformation axis is shown by the dashed line in Fig. 2(a). The coordinates in the ZQ-plane, i.e., z_i's, can be found by solving the system of nonlinear equations numerically. With the new coordinates, the overall air capacitance is given by [7]

$$C_{Q\rm air} = \epsilon_0\,\frac{K(k')}{K(k)} \quad k = \frac{z_3 + z_4}{z_3 + z_1}\sqrt{\frac{(z_1 + z_3)^2 - (z_3 - z_1)^2}{(z_3 + z_4)^2 - (z_3 - z_1)^2}}\,. \tag{7}$$

To view this capacitance as a sum of several contributions from ideal sources turns out to be very useful; therefore, $C_{Q\rm air}$ is viewed as consisting of three components, as illustrated in Fig. 2(c) (subscript Q stands for quarter-plane and "air" denotes that the particular capacitance is air capacitance) in the rest of this paper.

- $C_{HQ\rm air}$ due to the horizontal surfaces

$$C_{HQ\rm air} = \epsilon_0\,\frac{K(k')}{K(k)}, \qquad \text{with } k = \frac{c}{b}\sqrt{\frac{b^2 - a^2}{c^2 - a^2}}\,. \tag{8}$$

- $C_{CQ\rm air}$ due to corners of the structure

$$C_{CQ\rm air} = C_{Q\rm air} - (C_{HQ\rm air} + C_{VQ\rm air}). \tag{9}$$

- $C_{VQ\rm air}$ due to vertical walls

$$C_{VQ\rm air} = t/2s, \qquad \text{where } s = (b-a)/2. \tag{10}$$

For practical dimensions $C_{CQ\rm air}$ is a small contribution to the overall capacitance; nevertheless, for higher accuracy, it should be taken into account. The change in $C_{CQ\rm air}$ can be approximated using the following relation, which is obtained by curve-fitting several points:

$$\tilde{C}_{CQ\rm air} = 0.03\epsilon_0\Big(1 - \exp(-5t/s)\Big). \tag{11}$$

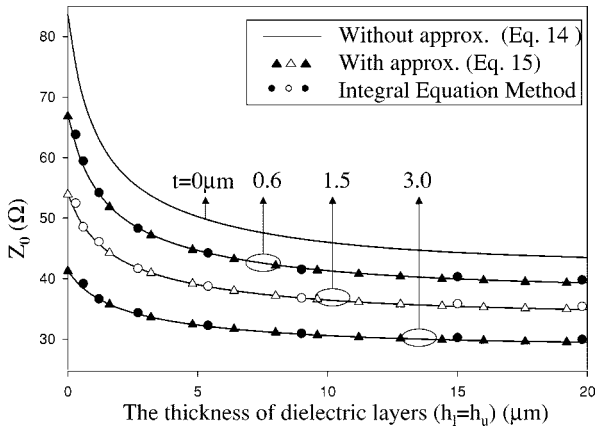

Fig. 3. Calculated Z_0 for symmetric CPW's (t in micrometers).

C. Capacitance of a Finite-Thickness CPW Encapsulated in a Dielectric Membrane

Following the partial capacitances concept introduced in the previous section, the contribution corresponding to the capacitance between horizontal surfaces of the conductors can be found by using the capacitance function. The horizontal capacitance for one quadrant (with zero-thickness, but the same horizontal dimensions) is expressed as

$$C_{HQ} = \frac{1}{2} C(h,\, \epsilon_1) \tag{12}$$

where h is the thickness of the dielectric layer. The capacitance due to corner discontinuity, i.e., C_{CQ}, requires extensive calculations. For practical systems when h and t are comparable, we can assume that all the fields are effectively in the dielectric layer. As a result, C_{CQ} and C_{VQ} are written as

$$C_{CQ} \approx \epsilon_1 C_{CQ\mathrm{air}} \quad C_{VQ} = \epsilon_1 C_{VQ\mathrm{air}}. \tag{13}$$

D. Total Capacitance

The seminumerical approach can be summed in the following capacitance formulas:

$$C_{\mathrm{air}} = 4C_{Q\mathrm{air}}$$
$$C_{\mathrm{total}} = \Big[C(h_u,\, \epsilon_1) + C(h_l,\, \epsilon_1)\Big] + 4\epsilon_1 \left[C_{Q\mathrm{air}} - \epsilon_0 \frac{K(k')}{K(k)}\right]. \tag{14}$$

In the above equations, k is as given in (8). However, in these formulas, the calculation of C_{air} requires the solution of a system of nonlinear equations; instead, if $C_{CQ\mathrm{air}}$ is approximated as in (11), then closed-form analytic expressions are obtained by substituting $C_{Q\mathrm{air}}$ in (14) as follows:

$$\tilde{C}_{Q\mathrm{air}} = \epsilon_0 \left[\frac{K(k')}{K(k)} + \frac{t}{a-b} + 0.03\Big(1 - \exp(-5t/s)\Big)\right]. \tag{15}$$

III. Discussion of the Results

The capacitance and characteristic impedance were computed for various values of a, b, c, t, and h analytically [using (15)], seminumerically [using (14)], and numerically (using the integral-equation method). In Fig. 3, the characteristic impedance of micromachined CPW's as a function of t and h for $a = 24\,\mu$m, $b = 30\,\mu$m, and $c = 130\,\mu$m is shown.

TABLE I
Comparison of Computed and Measured Results. Dimensions are in Micrometers and Capacitances are in Picofarads/Centimeters

	Set #1	Set#2	Set #3
a	24	60	60
b	30	68	68
c	130	300	300
t	0.6	1.75	1.15
h_u	1.65	1.0	1.0
h_l	1.45	1.45	1.45
ϵ_1	3.9	3.9	3.9
C_{total} (Eq. 14)	0.924	1.039	0.934
C_{total} (Eq.15)	0.928	1.040	0.936
C_{total} (IE)	0.964	1.069	0.948
C_{total} (meas.)	0.86±0.02	1.14±0.02	0.93±0.02

The effect of conductor thickness on the characteristic impedance was observed while t/s changes from 0.1 to 0.5. The comparison of the results in Fig. 3 indicates very good agreement in the range of interest. In these figures, we also included the zero-thickness conductor limiting case. The error in characteristic impedance calculation can be more than 100% in some cases depending on the physical parameters of the system, if the conductor thickness is neglected. In the current CMOS fabrication processes, the dielectric film thicknesses for the micromachining purposes lie in the steepest part of the curves; therefore, the processes variations can affect the final result substantially.

We also present measurement results along with computation results for three different structures in Table I.

A seminumerical and an analytical quasi-TEM formulation for a lossless micromachined CPW system has been presented in this paper. The isolation criterion gave a reliable tool to minimize the effect of remaining silicon on the operation of micromachined CMOS CPW's. The errors introduced with this criterion are significantly smaller than the ones due to variation in process parameters.

References

[1] *IEEE Trans. Microwave Theory Tech. (Special Issue on Innovative Integration Techniques for Microwave and Millimeter-Wave Circuits)*, vol. 48, Nov. 1998.
[2] V. Milanović, M. Gaitan, E. D. Bowen, and M. E. Zaghloul, "Micromachined coplanar waveguides in CMOS technology," *IEEE Trans. Microwave Theory Tech.*, vol. 45, pp. 630–635, 1997.
[3] W. Heinrich, "Quasi-TEM description of MMIC coplanar lines including conductor-loss effects," *IEEE Trans. Microwave Theory Tech.*, vol. 41, pp. 45–52, Jan. 1993.
[4] R. E. Collin, *Foundations for Microwave Engineering*, 2nd ed. New York: McGraw-Hill, 1992.
[5] K. C. Gupta, R. Garg, I. Bahl, and P. Bhartia, *Microstrip Lines and Slotlines*, 2nd ed. Norwood, MA: Artech House, 1996.
[6] C. P. Wen, "Coplanar waveguide: A surface strip transmission line suitable for nonreciprocal gyromagnetic device applications," *IEEE Trans. Microwave Theory Tech.*, vol. MTT-17, pp. 1087–1090, Dec. 1969.
[7] C. Veyres and V. F. Hanna, "Extension of the application of conformal mapping techniques to coplanar lines with finite dimensions," *Int. J. Electron.*, vol. 48, pp. 47–56, 1980.
[8] G. Ghione, "A CAD-oriented analytical model for the losses of general asymmetric coplanar lines in hybrid and monolithic MIC's," *IEEE Trans. Microwave Theory Tech.*, vol. 41, pp. 1499–1510, Sept. 1993.
[9] C. Chang, W. Chang, and C. Chen, "Full-wave analysis of multilayer coplanar lines," *IEEE Trans. Microwave Theory Tech.*, vol. 39, pp. 747–750, Apr. 1991.

Remote Millimeter-Wave Beam Control by the Illumination of a Semiconductor

G. F. Brand

***Abstract*—The aim of this paper is to use diffraction gratings, produced by projecting a grating pattern onto a semiconductor wafer from a remote location, to control the direction of a reflected beam. We find the conditions for which diffraction at the specular angle is small so that most of the radiation goes into adjacent interference maxima whose directions may be controlled by changing the period of the projected pattern. Some preliminary experiments are reported.**

***Index Terms*—Diffraction, gratings, millimeter-wave devices, optical control, photoconductivity, solid-state plasmas.**

I. Earlier Work

A diffraction grating can be produced by projecting a grating pattern onto a semiconductor wafer. Where the light falls, the conductivity is high because of the formation of a photo-induced electron–hole plasma, elsewhere the conductivity remains low. Diffraction experiments have been reported previously using a mask with fixed period located close to the semiconductor [1], [2], and using optical fibers to convey laser light to the semiconductor [3]. Our projection method allows the period of the grating and, hence, the directions of the interference maxima, to be changed simply by moving distant optical components. We reported in an earlier paper a transmission experiment [4] in which a millimeter-wave beam was diffracted as it passed through such a grating. However, in that experiment, most of the beam proceeded in the straight-through direction, only a small fraction was diffracted to the sides. In this paper, we describe a reflection experiment where most of the beam is diffracted into the interference maxima whose directions can be controlled.

II. Reflection Grating

The principle can be illustrated by calculating the Fraunhofer diffraction pattern obtained when a plane wave is reflected from an ideal grating made of strips of two types of material with reflection coefficients ρ_1 and ρ_2. If the grating is made up of N (N is even) strips of the same width of each type of material and the period is D, then the intensity of the diffracted beam in the direction ϕ can be written, in the Fraunhofer approximation, as

$$I(\phi) = \frac{I_0}{4}\left(\frac{\sin\, ks\frac{D}{4}}{ks\frac{D}{4}}\right)^2\left(\frac{\sin\, ks\frac{ND}{2}}{N\,\sin\, ks\frac{D}{2}}\right)^2 \cdot\left|\rho_1\,\exp\left(-jks\frac{D}{4}\right)+\rho_2\,\exp\left(jks\frac{D}{4}\right)\right|^2 \quad (1)$$

where k is the wavenumber and $s = \sin\,\theta - \sin\,\phi$, in which θ is the angle of incidence and ϕ is the angle of diffraction.

Manuscript received January 27, 1999. This work was supported by the Australia Research Council, by the University of Sydney, and by the Science Foundation for Physics, University of Sydney, Sydney, Australia.

The author is with the School of Physics, University of Sydney, Sydney, NSW 2006, Australia (e-mail: brand@physics.usyd.edu.au).

Publisher Item Identifier S 0018-9480(00)03753-4.

The directions of the interference maxima are given by $ks(D/4) = m(\pi/2)$ (m integer). Substituting in (1) gives the intensities in the following directions:

$$\begin{aligned} &I = \frac{I_0}{4}|\rho_1+\rho_2|^2, \qquad \text{if } m = 0\\ &I = 0, \qquad \text{if } m \text{ is even, not } 0\\ &I = \frac{I_0}{4}\left(\frac{2}{m\pi}\right)^2|\rho_1-\rho_2|^2, \qquad \text{if } m \text{ is odd.} \end{aligned} \quad (2)$$

Note that $m = 0$ corresponds to the case $\phi = \theta$, i.e., reflection at the specular angle.

The ideal grating, for our present purpose, would have: 1) zero intensity at the specular angle; in other words, no reflection in that direction and 2) greatest intensity in the directions of the adjacent interference maxima. This could be achieved if we could create strips with $\rho_2 = -\rho_1$. Then, $|\rho_1 + \rho_2| = 0$ and $|\rho_1 - \rho_2| = 2\rho_1$.

In Section III, we consider reflections from a silicon wafer, when it is dark and when it is illuminated, to see how close we can come to this ideal situation.

III. Diffraction Calculations

Suppose plane waves described by $\exp\, j(kr-\omega t)$ are incident at an angle θ on a wafer of thickness l. The reflection and transmission coefficients for the perpendicular polarization, found by applying Fresnel's equations [5] are

$$\begin{aligned} \rho &= \frac{(1-\tilde{n}^2\tilde{\alpha}^2)\Big(\exp(j2k\tilde{n}\,\cos\,\tilde{\theta}'l)-1\Big)}{(1-\tilde{n}\tilde{\alpha})^2\,\exp(j2k\tilde{n}\,\cos\,\tilde{\theta}'l)-(1+\tilde{n}\tilde{\alpha})^2}\\ \tau &= -\frac{4\tilde{n}\tilde{\alpha}\,\exp\Big(jk(\tilde{n}\,\cos\,\tilde{\theta}'-\cos\,\theta)l\Big)}{(1-\tilde{n}\tilde{\alpha})^2\,\exp(j2k\tilde{n}\,\cos\,\tilde{\theta}'l)-(1+\tilde{n}\tilde{\alpha})^2} \end{aligned} \quad (3)$$

where $\tilde{n}$ is the complex refractive index. The relations linking the various complex and real quantities are

$$\varepsilon = \varepsilon_r + j\frac{\sigma}{\varepsilon_0\omega} = \tilde{n}^2 = (n+j\kappa)^2$$

where ε_r is the real part of the permittivity (for silicon $\varepsilon_r = 11.8$), σ is the conductivity, and ω is the angular frequency. In (3), $\tilde{\theta}'$ is the complex angle of propagation in the wafer and $\tilde{\alpha} = \cos\,\tilde{\theta}'/\cos\,\theta$. The corresponding expressions for the parallel polarization may be obtained by replacing $\tilde{n}\tilde{\alpha}$ by $\tilde{n}/\tilde{\alpha}$ and ρ by $-\rho$.

If the semiconductor is backed by a perfect conductor, the reflection coefficient for the perpendicular polarization is

$$\rho = \frac{(1+\tilde{n}\tilde{\alpha})\,\exp(j2k\tilde{n}\,\cos\,\tilde{\theta}'l)-(1-\tilde{n}\tilde{\alpha})}{(1-\tilde{n}\tilde{\alpha})\,\exp(j2k\tilde{n}\,\cos\,\tilde{\theta}'l)-(1+\tilde{n}\tilde{\alpha})}. \quad (4)$$

The grating is made up of strips that are not illuminated with reflection coefficient ρ_1 (calculated using $\sigma_1 = 0$) and the strips that are, ρ_2. A value for ρ_2 exactly equal to $-\rho_1$ is unattainable; the best that can be achieved is to have $|\rho_1 + \rho_2|$ as low as possible and $|\rho_1 - \rho_2|$ as high as possible. In a situation similar to our experiment, where the incident plane wave is perpendicularly polarized, strikes at an angle of $\theta = 20^\circ$ and has a frequency of 105 GHz (wavelength 2.86 mm), the best results would be obtained when the silicon wafer had a conductor backing and the thickness l was 0.63 mm.

Fig. 1 shows two representative Fraunhofer diffraction patterns, calculated using (1) for two different levels of illumination. The incident wave is the same as above, the wafer thickness $l = 0.63$ mm and the period of the pattern $D = 20$ mm. When the illumination is weak and the conductivity is low ($\sigma_2 = 2$ S m^{-1}), the diffracted signal remains small and most of the beam is specularly reflected at $\phi = 20^\circ$

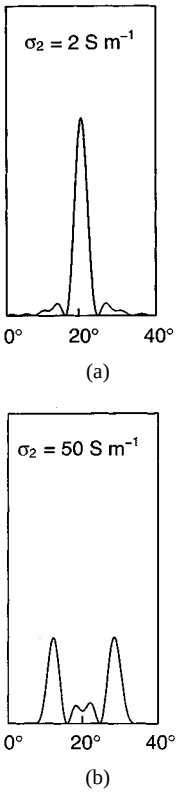

Fig. 1. Fraunhofer diffraction (intensity versus ϕ) on reflection from a strip grating for two representative values of σ_2 of the illuminated regions.

[see Fig. 1(a)]. On the other hand, when the illumination is strong and the conductivity is high ($\sigma_2 = 50$ S m^{-1}), the diffracted signals at $\phi = 11.5^\circ$ and $\phi = 29.0^\circ$ greatly exceed the specular reflection [see Fig. 1(b)].

In this simple treatment, the conductivity is taken to be uniform from the front to the back face of the silicon. A more complete treatment would take into account the generation of electron–hole pairs close to the illuminated surface, diffusion into the silicon, and recombination near the surface.

IV. Experiment

The experimental arrangement is shown in Fig. 2. The light source was a pulsed arc lamp (Oriel Series Q flash lamp with a 5-J xenon bulb and typical pulse length of 9 μs). The pattern in the cutout mask had clear and opaque regions of equal width and a period $D' = 8$ mm. The mask and lens (focal length 133 mm) were placed so the projected pattern had a period $D = 20$ mm. The millimeter-wave source was a 105-GHz IMPATT solid-state oscillator. It was located 500 mm from the wafer, the incident beam was perpendicularly polarized, and the angle of incidence was $\theta = 20^\circ$. One W-band horn and detector was mounted in a fixed position to monitor the specular reflection. A second horn was mounted on a stepper-motor-driven stage to scan along a line located 500 mm from the wafer, as shown in the figure. Diffraction took place from a circular region (diameter 50 mm). The area beyond was covered by microwave absorber.

The silicon wafer was n-type intrinsic with high resistivity 1000–3500 $\Omega \cdot$ cm (dark conductivity 0.10–0.03 S m^{-1}), a diameter of 76 mm, and a thickness of 0.38 mm. The conductor backing was copper. This value of thickness is much less then the preferred 0.63 mm. In order to obtain the required phase change on reflection from a dark region, a 0.58-mm layer of mylar was placed between the semiconductor and conductor backing.

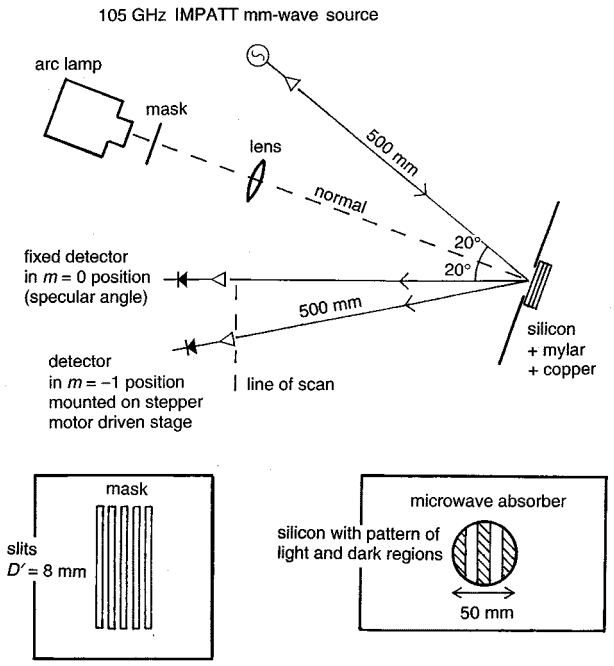

Fig. 2. Experimental arrangement.

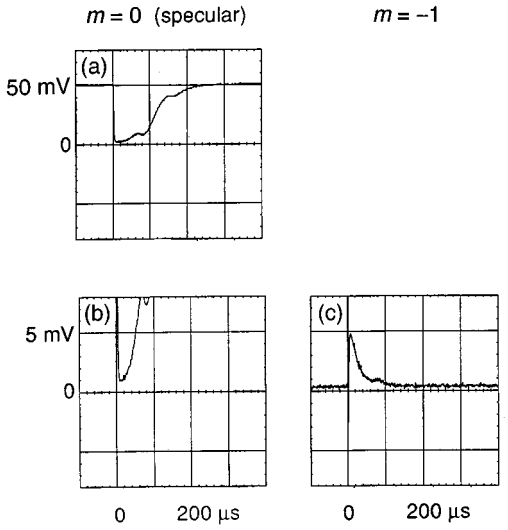

Fig. 3. Signal versus time when the light pattern is projected onto semiconductor. (a) and (b) At the $m = 0$ position. (c) At the $m = -1$ position.

Fig. 3 shows the time variation of the reflected signals when a light pattern is projected onto the semiconductor. The specularly reflected signal ($m = 0$) is shown at two scales [see Fig. 3(a) and (b)]. The signal diffracted into the first interference maximum ($m = -1$, 78 mm away) is shown in Fig. 3(c). A comparison of the traces in Fig. 3(b) and (c), plotted with the same scale, demonstrate that when there is a projected pattern and the light intensity is a maximum, the $m = -1$ signal greatly exceeds the $m = 0$ signal. No signal is observed in the $m = -1$ direction when the pattern is absent.

Our diffracting object is not infinite in extent and our source and detector are quite close, so it is not surprising that the diffraction depends on exactly how the pattern of light and dark regions falls within the circular boundary. Fig. 4 shows how the diffraction pattern in the vicinity of the first interference maximum is observed to vary as the shadow

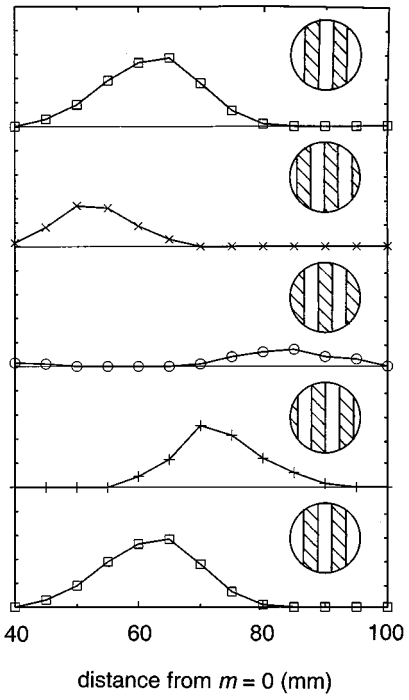

Fig. 4. Scans of the diffraction patterns in the vicinity of $m = -1$ as the shadow pattern is translated across the silicon wafer. The insets show the shadow patterns.

pattern is translated across the silicon wafer. Calculations show this behavior to be expected.

Blurring of the grating edges due to sideways diffusion of the carriers is estimated to be less than 1 mm under the conditions of this experiment.

Similar results were obtained when the silicon was illuminated from the rear. The copper conductor was replaced by a 100 wires per inch nickel mesh. This mesh, with a reflectance of 0.96 at 105 GHz, reflected the millimeter waves, but allowed light to pass through.

In conclusion, the experiments described here have demonstrated that a diffraction grating, produced by projecting a grating pattern onto a semiconductor wafer, can redirect a millimeter-wave beam. The new direction being determined largely by the period of the projected pattern. A measure of fine control over the direction can be achieved by translating the pattern across the wafer.

ACKNOWLEDGMENT

The author would like to thank J. Lizier for his assistance in carrying out the investigation in which the silicon wafer was illuminated from the rear.

REFERENCES

[1] V. A. Manasson, L. S. Savodnik, A. Moussessian, and D. B. Rutledge, "Millimeter-wave diffraction by a photo-induced plasma grating," *IEEE Trans. Microwave Theory Tech.*, vol. 43, pp. 2288–2290, Sept. 1995.

[2] V. A. Manasson, L. S. Sadovnik, P. I. Schnitser, and R. Mino, "Millimeter-wave optically scanning antenna based on photoinduced plasma grating," *Opt. Eng.*, vol. 35, pp. 357–361, 1996.

[3] W. Platte, "LED-induced distributed Bragg reflection microwave filter with fiber-optically controlled change of center frequency in photoconductivity gratings," *IEEE Trans. Microwave Theory Tech.*, vol. 39, pp. 359–363, Feb. 1991.

[4] G. F. Brand, "Diffraction of millimeter waves by projecting a shadow pattern onto a semiconductor," *Int. J. Infrared Millimeter Waves*, vol. 17, pp. 1253–1262, 1996.

[5] P. Lorrain and D. Corson, *Electromagnetic Fields and Waves*, 2nd ed. San Francisco, CA: Freeman, 1970, p. 508 ff.

A Distributed-Feedback Antenna Oscillator

Shin-Lin Wang, Young-Huang Chou, and Shyh-Jong Chung

***Abstract*—In this paper, a new design of the active transmitting antenna array, called the distributed-feedback antenna oscillator, is proposed. The active array is formed by serially connecting several unit cells to a closed loop. Each unit cell contains an amplifier and a two-port antenna, with an overall insertion gain larger than 0 dB and a phase delay equal to a multiple of 360°. The signal traveling on the loop is amplified and radiated in each unit cell. The radiation fields from all the antennas are then combined in free space. A four-element feedback antenna oscillator operating at 10 GHz is demonstrated by using two-port aperture-coupled microstrip antennas. Simulation results show that multiple oscillation modes with different frequencies and different radiation beams may be excited in the antenna oscillator. By experiment, it is found that each oscillation mode can be built by tuning the biases of the oscillator. The measured radiation pattern for each mode agrees very well with the predicted one. For a single-mode operation with a broadside pattern, bandstop filters of a simple geometry are designed and embedded in the oscillator to suppress the unwanted oscillation modes. Finally, the influence of the bias condition on the radiation power of the single-mode oscillator is investigated.**

***Index Terms*—Active antenna, feedback, oscillator, spatial power combining.**

I. INTRODUCTION

Due to the advantages of compact sizes, low weights, and low costs, active transmitting antennas have attracted much attention in the applications of communication and radar systems at the microwave and millimeter-wave frequencies [1]–[3]. By integrating a passive planar antenna with solid-state devices, the active transmitting antenna performs not only as a radiator, but also as an oscillator. The design of an active antenna is essentially that of an oscillator, which could be mainly grouped into two types, i.e., the negative-resistance and feedback types. In the first type, a two-terminal device (IMPATT or Gunn diode) [4] or a three-terminal device [MESFET or high electron-mobility transistor (HEMT)] [5] was first used to create a negative-resistance one-port. The antenna with a suitable input resistance was then connected to the one-port as a radiation load. In the feedback type, a two-port antenna was generated and connected to a pre-designed amplifier [6], [7]. The signal coming from the output of the amplifier was fed to one port of the antenna. With most of the signal power radiated to free space, some of it was coupled out through the second port of the antenna, which was then fed to the amplifier's input. In this design type, the antenna possessed the function of a feedback resonator. To start the oscillation,

Manuscript received February 2, 1999. This work was supported by the Ministry of Education and by the National Science Council, R.O.C., under Contract 89-E-FAO6-2-4.

The authors are with the Department of Communication Engineering, National Chiao Tung University, Hsinchu 300 Taiwan, R.O.C. (e-mail: sjchung@cm.nctu.edu.tw).

Publisher Item Identifier S 0018-9480(00)03754-6.

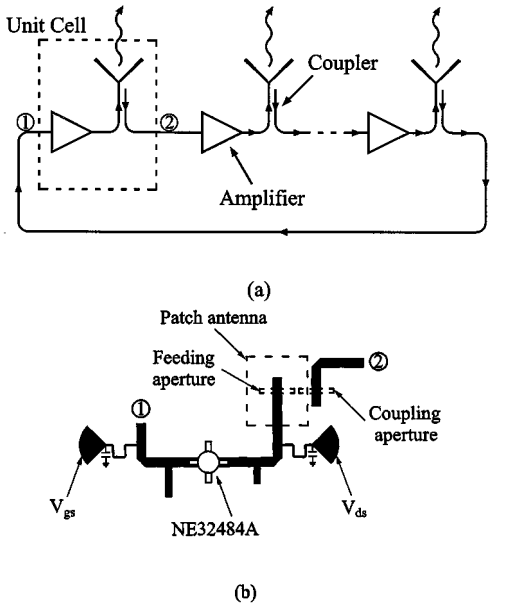

Fig. 1. (a) Conceptual diagram of the distributed feedback antenna oscillator. (b) Circuit layout of a unit cell using the two-port aperture-coupled microstrip antenna.

the closed-loop small-signal gain should be larger than 1–2 dB and the electrical length of the loop should be a multiple of 360°.

By forming several active antennas as an array, the powers radiated from the antennas can spatially combine in free space, resulting in a high output power. This spatial power-combining technique can solve the problems of limited available powers from solid-state devices and high propagation losses in transmission lines, especially for millimeter-wave systems. To stably synchronize the oscillating frequencies of the active antennas, strong injection-locking signals should be applied to the antenna oscillators. These injection signals may come from the mutual couplings between oscillators through an embedded mutual-coupling network [8] or be supplied by an external stable source through a feeding network [9], [10].

In this paper, we propose a new design of active transmitting antennas, called the *distributed-feedback antenna oscillator*, as shown in Fig. 1(a). This design is actually an extension of the feedback-type active antenna, which is formed by serially connecting several unit cells to a closed loop. Each unit cell contains an amplifier and a two-port antenna, with an overall insertion gain larger than 0 dB and a phase delay equal to a multiple of 360°. This structure can be viewed as a strong coupling active antenna array. The signal traveling on the loop is amplified and radiated in each unit cell. The radiation fields from all the antennas are then combined in free space.

II. Design and Simulation

A symmetrical four-element (2 × 2) distributed-feedback antenna oscillator operating at 10 GHz is demonstrated using the unit cell, as shown in Fig. 1(b). The antenna used is a two-port aperture-coupled microstrip antenna [7]. The antenna patches were fabricated on a substrate of $\varepsilon_r = 2.33$ and $h = 31$ mil (thickness) and the amplifier circuits were on a substrate of $\varepsilon_r = 2.2$ and $h = 20$ mil. The signal was fed to the antenna patch through the feeding aperture on the ground plane separating the two substrates and was coupled back to the circuit layer through another aperture under the same patch. The two-port microstrip antenna was designed to be with a transmission loss (due to the radiation of the patch) of 8.5 dB at the center frequency of 10 GHz and a 10-dB return-loss bandwidth of 3.6%. The amplifier designed using an NE32484A HEMT possessed a small-signal gain of about 10 dB at 10 GHz. Note that, by using the two-port aperture-coupled microstrip antennas, no dc block capacitors were needed to isolate the amplifiers' biases. The antenna spacing of the oscillator was set to be 0.6 λ_0 at the design frequency. The whole oscillator was simulated using the harmonic-balance method by the commercial software HP Series IV. In the simulation, the free-space mutual coupling between antennas was neglected.

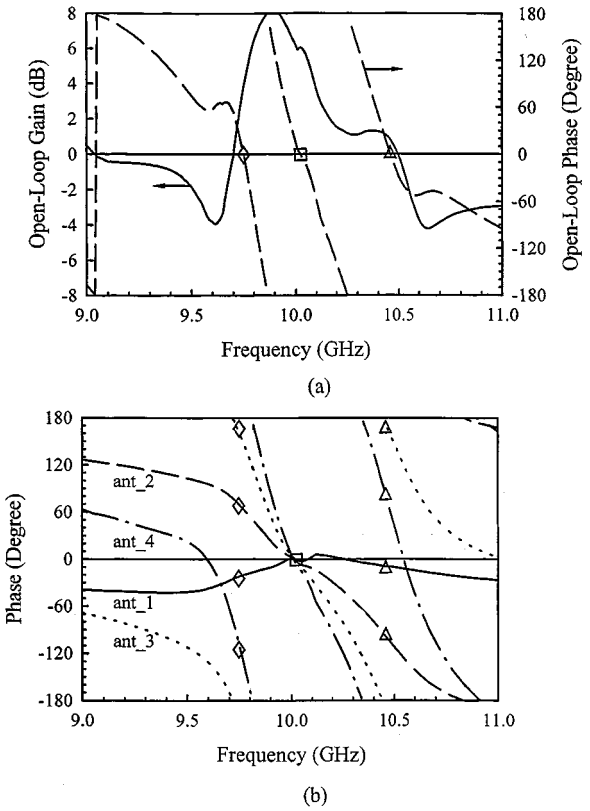

Fig. 2. Simulation results of the four-element antenna oscillator at $V_{ds} = 2$ V and $V_{gs} = -0.3$ V. (a) Open-loop gain and phase as functions of frequency. (b) Antenna signal phases as functions of frequency.

Fig. 2(a) depicts the simulated small-signal open-loop gain and phase as functions of the frequency. The amplifiers' biases were set to be $V_{ds} = 2$ V and $V_{gs} = -0.3$ V. As shown, the loop gain is larger than 0 dB in the frequency band from 9.7 to 10.5 GHz. Within this band, three zero crossing points of the phase curve happen at the frequencies of 9.75, 10.02, and 10.46 GHz, with corresponding loop gains of 3.3, 5.8, and 1 dB, respectively. This means that the circuit may oscillate at these three frequencies since both the gain and phase satisfy the requirements to start the oscillation. It is interesting to look at the signal phases at the four antennas. Simulation results depicted in Fig. 2(b) show that the antennas produce in-phase radiation fields when the circuit oscillates at 10.02 GHz. However, when the oscillation happens at 10.46 GHz (9.75 GHz), a 90° phase delay (advance) occurs between adjacent antennas.

III. Measurement

The designed 2 × 2 feedback oscillator was fabricated and measured. An X-band horn antenna with an HP 8564E spectrum analyzer was used to detect the radiation fields from the antenna array. During measuring, the amplifiers' gate bias (V_{gs}) was first fixed at −0.3 V and the drain bias (V_{ds}) was then gradually increased from 0 V. As V_{ds} approached 2 V, the active array oscillated at one of the two frequencies

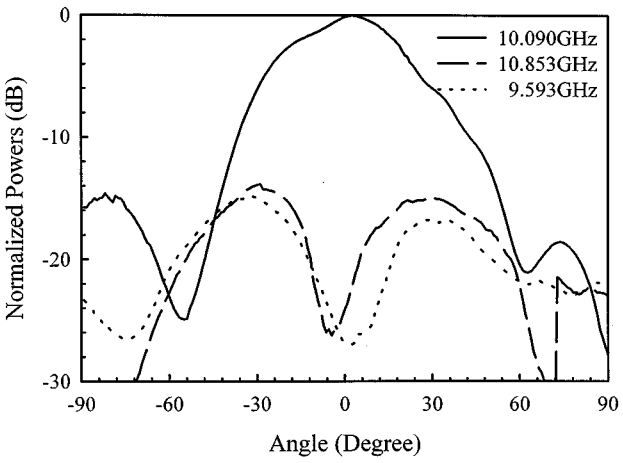

Fig. 3. Measured radiation patterns of the four-element antenna oscillator at the frequencies of 10.090 GHz ($V_{\rm ds} = 3.72$ V), 10.853 GHz ($V_{\rm ds} = 2$ V), and 9.593 GHz ($V_{\rm ds} = 2$ V). The gate bias $V_{\rm gs}$ is fixed at -0.3 V.

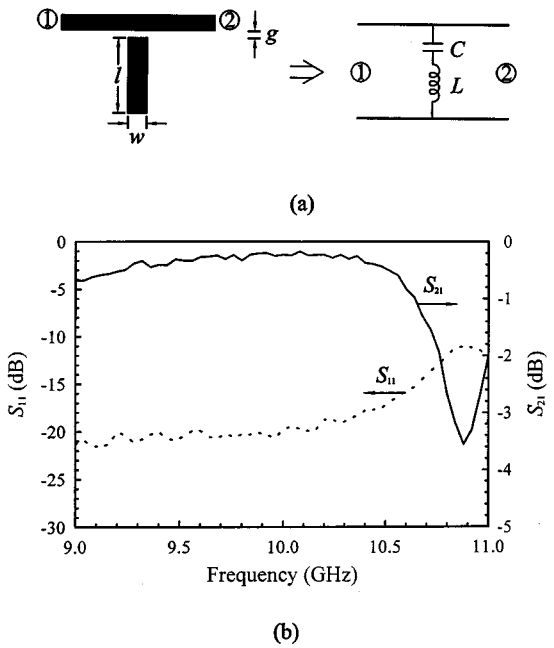

Fig. 4. (a) Configuration and equivalent circuit of the bandstop filter. (b) Measured scattering parameters of a 10.85-GHz bandstop filter with $l = 9.05$ mm, $w = 3$ mm, and $g = 0.1$ mm.

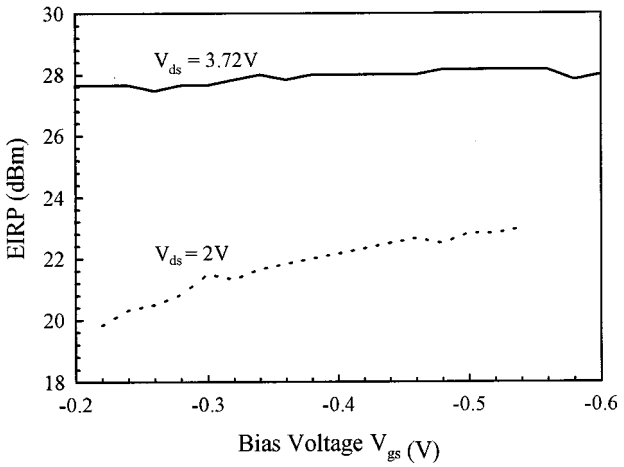

Fig. 5. Variations of the EIRP's as functions of the gate bias $V_{\rm gs}$, for the filter-embedded oscillator with $V_{\rm ds} = 3.72$ and 2 V.

of 10.85 and 9.59 GHz. We were unable to determine which oscillating frequency was generated first. The oscillation depended on the process of changing the drain bias. However, when $V_{\rm ds}$ was further increased near 3.72 V, the oscillating frequency jumped to 10.09 GHz. Further increase of the bias did not change the oscillating frequency. Thus, as predicted in the simulation results, the fabricated four-element antenna oscillator possessed three oscillating frequencies, i.e., 9.59, 10.09, and 10.85 GHz. The deviations of the measured frequencies to the simulated ones are 1.6%,, 0.7%,, and 3.7%, respectively. Fig. 3 illustrates the measured radiation patterns at these frequencies. It is obvious that an in-phase pattern was obtained at 10.09 GHz, which agreed with the corresponding simulation result at 10.02 GHz. Also, as shown in Fig. 2(b), the simulated antenna phase differences at the other two oscillating frequencies are 90° (9.75 GHz) and -90° (10.46 GHz), both corresponding to a radiation pattern with maxima located at $\pm 34^\circ$. Comparing to the experiment results, the radiation patterns at 9.59 and 10.85 GHz, shown in Fig. 3, have the maximum powers appeared at about $\pm 30^\circ$, which are very close to the simulations.

For many applications, an active array with a single stable oscillating frequency and a broadside radiation pattern is needed. To this end, filters with a very narrow stopband may be embedded in the oscillator loop to reject the unwanted oscillating frequencies. These filters should possess a simple geometry to make the design of the whole oscillator compact. Also, they should provide enough attenuation to the unwanted frequencies, while having little influence on the signal propagation at the desired frequency. To fulfill these requirements, the filter structure shown in Fig. 4(a) was used in this investigation. The filter was completed by simply putting an open-ended microstrip stub in the proximity of a microstrip section in the oscillator loop. The stub length l was designed slightly smaller than half of the guided wavelength at the oscillating frequency to be eliminated so that the stub's input impedance was inductive, with the inductance L varying fast near the unwanted frequency. The gap between the stub and microstrip loop section behaved as a capacitor, with the capacitance C depending on the gap length g and the gapwidth (or stub width) w. Thus, the equivalent circuit of this filter was a series *LC* resonator shunted to the microstrip line, as shown in Fig. 4(a). By suitably choosing l, g, and w, the *LC* circuit could be designed to resonate and, thus, be shorted, at the unwanted frequency. Since the stub inductance *L* changes rapidly with the frequency, the stopband of the filter would be very narrow. Fig. 4(b) illustrates the measured scattering parameters for a bandstop filter designed at 10.85 GHz. As is shown, the insertion loss S_{21} of this filter is -3.6 dB at 10.85 GHz, but is only -0.2 dB around 10 GHz. Another filter (with $l = 10.3$ mm, $w = 3$ mm, and $g = 0.1$ mm) has also been designed at 9.59 GHz. The measured results showed an insertion loss of -3.5 dB at 9.59 GHz and -0.3 dB around 10 GHz.

Both the 10.85- and 9.59-GHz bandstop filters were added in the circuit loop. The experiment showed that the original oscillating signals at 10.85 and 9.59 GHz were effectively eliminated. The active array stably oscillated at a frequency around 10.08 GHz when $V_{\rm ds}$ was changed from 2 to 3.72 V, with the radiation beam pointed to the broadside direction. Fig. 5 depicts the variations of the effective isotropic radiation power (EIRP) as functions of the bias voltages. For a fixed gate bias of $V_{\rm gs} = -0.3$ V, when the drain bias was raised from 2 to 3.72 V, the EIRP was enhanced by 6.1 dBm (from 21.5 to 27.6 dBm). However, contrary to these large EIRP variations, the change of the gate bias caused limited variations of the EIRP. For the active devices (i.e., HEMT's) used, at a fixed drain voltage $V_{\rm ds}$, the more negative is the

gate bias $V_{\rm gs}$, the smaller the drain current I_d is and, thus, the lower the dc power ($=V_{\rm ds}I_d$) is consumed. Therefore, the dc-to-RF efficiency can be improved by applying a more negative $V_{\rm gs}$ without disturbing the EIRP significantly.

IV. Conclusions

In this paper, a distributed feedback oscillator with multiple antenna elements has been proposed and implemented at frequencies near 10 GHz. By using the commercial software HP Series IV, the multielement oscillator has been simulated, which showed that the oscillator possessed multiple oscillating frequencies, with each frequency corresponding to a different array radiation pattern. The experiments also confirmed the existence of these frequencies. It was found that the oscillation could be built at one of these oscillating frequencies by changing the biases of the oscillator. For each oscillating frequency, the radiation pattern has also been measured, which agreed very well with the predicted one. In order to attain a single oscillating frequency with a broadside radiation pattern, narrow stopband filters with a simple geometry have been designed and embedded in the oscillator to suppress the unwanted oscillation modes. The measurement verified the efficacy of these filters. For the filter-embedded antenna oscillator, the variation of the EIRP with respect to the change of the bias voltages was measured and compared. The results showed that the increase of the drain bias could effectively raise the EIRP, while that of the gate bias did not change it much. Thus, the dc-to-RF efficiency could be enhanced by using a negative gate bias with a higher voltage. In the future, several multielement antenna oscillators developed in this paper can be suitably arranged into a large active array. By means of the free-space mutual couplings between antennas or external injection signals, the radiated fields from all the oscillators may be coherently combined to create a high output power.

References

[1] J. A. Navarro and K. Chang, *Integrated Active Antennas and Spatial Power Combining*. New York: Wiley, 1996.

[2] B. A. York and Z. B. Popović, *Active and Quasi-Optical Arrays for Solid-State Power Combining*. New York: Wiley, 1997.

[3] Y. Qian and T. Itoh, "Progress in active integrated antennas and their applications," *IEEE Trans. Microwave Theory Tech.*, vol. 46, pp. 1891–1900, Nov. 1998.

[4] J. A. Navarro, F. Lu, and K. Chang, "Active inverted stripline circular patch antennas for spatial power combining," *IEEE Trans. Microwave Theory Tech.*, vol. 41, pp. 1856–1863, Oct. 1993.

[5] J. Birkeland and T. Itoh, "Two-port FET oscillators with applications to active arrays," *IEEE Microwave Guided Wave Lett.*, vol. 1, pp. 112–113, May 1991.

[6] R. D. Martinez and R. C. Compton, "High-efficiency FET/microstrip-patch oscillators," *IEEE Antennas Propagat. Mag.*, vol. 36, pp. 16–19, Feb. 1994.

[7] W.-J. Tseng and S.-J. Chung, "Analysis of a two-port aperture-coupled microstrip antenna," *IEEE Trans. Microwave Theory Tech.*, vol. 46, pp. 530–535, May 1998.

[8] R. A. York, P. Liao, and J. J. Lynch, "Oscillator array dynamics with broadband N-port coupling network," *IEEE Trans. Microwave Theory Tech.*, vol. 42, pp. 2040–2045, Nov. 1994.

[9] J. Birkeland and T. Itoh, "A 16-element quasi-optical FET oscillator power combining array with external injection locking," *IEEE Trans. Microwave Theory Tech.*, vol. 40, pp. 475–481, Mar. 1992.

[10] Y.-C. Yang, S.-J. Chung, and K. Chang, "Novel active antenna amplifying arrays," in *IEEE MTT-S Int. Microwave Symp. Dig.*, Baltimore, MD, June 1998, pp. 997–1000.

Modeling of Broad-Band Traveling-Wave Optical-Intensity Modulators

R. Krähenbühl and W. K. Burns

***Abstract*—In this paper, an accurate simulation tool for the electrical and optical response of broad-band traveling-wave optical intensity modulators is presented, which takes into account multisectional electrical transmission lines. This model is applied to analyze a high-speed fully packaged $LiNbO_3$ Mach–Zehnder interferometer.**

***Index Terms*—Intensity modulator, optical communication, simulation tool, traveling-wave devices.**

I. Introduction

High-speed traveling-wave (TW) broad-band optical intensity modulators are expected to play an important role in future communication systems. Efficient simulation tools are needed to shorten the time of their development, reduce their cost, and to improve their performance in the millimeter-wave frequency spectrum.

Previously, the optical performance of TW modulators have been modeled by considering microwave optical velocity mismatch [1], resistive electrode loss [2], and electrical reflections due to impedance mismatch between electrical connectors and the active device [3]. However, with the advent of fully packaged devices having multisectional electrical transmission lines, considerations such as electrode loss in nonactive sections, reflections from internal impedance transitions, and contributions from discontinuities between the high-frequency connector and electrical line have become very important.

The purpose of this paper is to provide a flexible model for the electrical and optical frequency-domain response of a broad-band TW optical-intensity modulator, by taking into account microwave loss and impedance transitions of the active and any number of nonactive electrical microwave segments. Both the electrical and optical frequency domains are obtained by considering the electrical transmission line as a multisectional microwave cavity. The electrical transmission and reflection responses of the device are directly given by the frequency responses of this microwave cavity. In addition, both amplitude and phase of the microwave-induced optical phase shift are obtained by iterative summation of all co-propagating and counter-propagating electrical waves within the active section of the microwave cavity and direct integration.

II. Microwave-Cavity Model for Optical and Electrical Response

The electrical performances of the microwave electrode in high-speed TW modulators are determined by a complex interplay of device and electrode geometry. This leads to different characteristic impedances and phase velocities in each section along the microwave electrode. To account for several line segments with different electrical characteristics, we treat the electrical transmission line of the modulator as a multisectional microwave cavity. In our considerations and

Manuscript received February 23, 1999. This work was supported by the Office of Naval Research Laboratory.

R. Krähenbühl is with Code 5671, Naval Research Laboratory, Washington, DC 20375 USA, and is also with VPI, Blacksburg, VA 24061 USA (e-mail: roger@ccf.nrl.navy.mil).

W. K. Burns is with Code 5671, Naval Research Laboratory, Washington, DC 20375 USA.

Publisher Item Identifier S 0018-9480(00)03755-8.

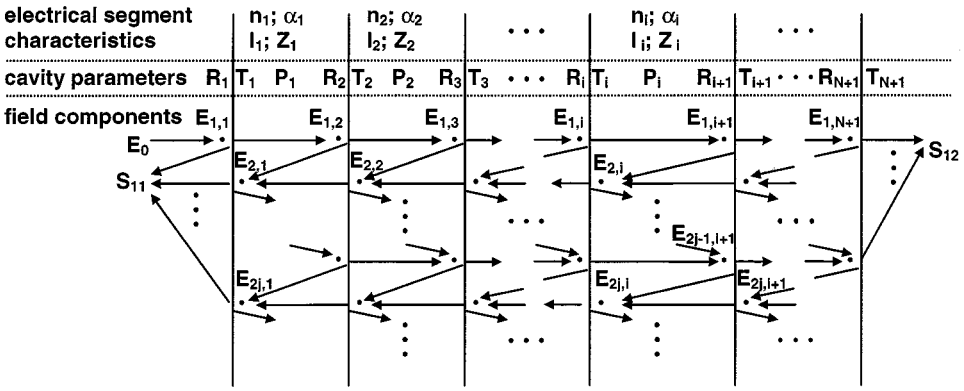

Fig. 1. Microwave-cavity model of a multisectional electronic transmission line with N segments, showing the first and jth round trip through the cavity.

calculations, we mainly follow the basic approach as given in [3], but extend it to the more general case of any number of nonactive sections. The basic assumptions underlying the development of the model may be described with reference to Fig. 1. An incident electromagnetic wave entering the cavity passes forward and backward inside the cavity, thereby undergoing different reflections, and transmissions at the segment interfaces, as well as different absorption and phase changes within the segments, until all power has left the cavity either as reflected or transmitted power. As shown in Fig. 1, the microwave electrode of the modulator is treated as a microwave cavity with field reflection coefficients (R_i) and field transmission coefficients (T_i) for the segment interfaces, as well as field propagation (P_i) within the corresponding segment. The reflection and transmission coefficients are represented by the characteristic impedances (Z_i) of two connecting segments as follows:

$$R_i = \frac{Z_i - Z_{i-1}}{Z_i + Z_{i-1}} \tag{1}$$

$$T_i = \frac{2 \cdot \sqrt{Z_i \cdot Z_{i-1}}}{Z_i + Z_{i-1}} \tag{2}$$

The field propagation (P_i), which describes the electrical loss and phase change in a section, is given by

$$P_i = e^{-\alpha_i \cdot l_i + i \cdot \beta_i \cdot l_i} \tag{3}$$

with section length l_i, microwave loss α_i, and characteristic phase constant β_i, which is given by

$$\beta_i = \frac{2\pi \cdot f \cdot n_i}{c}. \tag{4}$$

Here, f denotes frequency, c is the free-space velocity of light, and n_i is the microwave index. Referring to Fig. 1, the co-propagating electric-field component in front of the interface $i+1$ of the jth round trip is given by

$$E_{2j-1,i+1} = E_{2j-2,i} \cdot (-R_i) \cdot P_i + E_{2j-1,i} \cdot T_i \cdot P_i \tag{5}$$

whereas the counter-propagating electric-field component in front of the ith interface is given by

$$E_{2j,i} = E_{2j-1,i+1} \cdot R_{i+1} \cdot P_i + E_{2j,i+1} \cdot T_{i+1} \cdot P_i \tag{6}$$

which accounts for the fact that a difference of phase change of π occurs for the reflection of an electromagnetic wave entering the interface from opposite sides $(R' = -R)$. Equations (5) and (6) define all field components at any point of any round trip within the cavity, assuming the initial field $E_{1,1} = E_0$, as well as all $E_{0,i} = 0$, all $E_{2j,N+1} = 0$, and all $E_{2j+1,1} = 0$. The total reflected electrical power is obtained by summing all electric-field components, which leave the cavity on the input side

$$S_{11} = \left| E_{1,1} \cdot R_1 + \sum_{j=1}^{\infty} E_{2j,1} \cdot T_1 \right|^2 \tag{7}$$

whereas the total transmitted electrical power is all power, which leaves the cavity at the output side

$$S_{12} = \left| \sum_{j=1}^{\infty} E_{2j-1,N+1} \cdot T_{N+1} \right|^2. \tag{8}$$

To get the optical response as a result of the interaction of the microwave voltage, we have to consider the accumulated electric field in the active section $(i = \mathrm{as})$. The z-dependent electric field inside the active section ($z = 0$ at interface as) for any z is then obtained by summing all forward and backward propagating electromagnetic-field contributions therein as follows:

$$E(z) = \sum_{j=1}^{\infty} E_{2j-1,\mathrm{as}+1} \cdot e^{-\alpha_{\mathrm{as}} \cdot (z - l_{\mathrm{as}}) + i \cdot \beta_{\mathrm{as}} \cdot (z - l_{\mathrm{as}})} + \sum_{j=1}^{\infty} E_{2j,\mathrm{as}} \cdot e^{\alpha_{\mathrm{as}} \cdot z - i \cdot \beta_{\mathrm{as}} \cdot z}. \tag{9}$$

For a time-varying field at angular frequency ω, the voltage in the active section may be obtained from $E(z)$ as follows:

$$V(z,t) = \mathrm{Re}\left[V(z) \cdot e^{-i \cdot \omega \cdot t} \right] \tag{10}$$

where $V(z)$ is proportional to $E(z)$ in (9). $V(z,t)$ may be written as

$$\begin{aligned} V(z,t) = {} & \sum_{j=1}^{\infty} \mathrm{Re}\left[V_{2j-1,\mathrm{as}+1} \cdot e^{\alpha_{\mathrm{as}} \cdot l_{\mathrm{as}} - i \cdot \beta_{\mathrm{as}} \cdot l_{\mathrm{as}}} \right] \cdot e^{-\alpha_{\mathrm{as}} \cdot z} \\ & \cdot \cos(\beta_{\mathrm{as}} \cdot z - \omega \cdot t) \\ & - \sum_{j=1}^{\infty} \mathrm{Im}\left[V_{2j-1,\mathrm{as}+1} \cdot e^{\alpha_{\mathrm{as}} \cdot l_{\mathrm{as}} - i \cdot \beta_{\mathrm{as}} \cdot l_{\mathrm{as}}} \right] \cdot e^{-\alpha_{\mathrm{as}} \cdot z} \\ & \cdot \sin(\beta_{\mathrm{as}} \cdot z - \omega \cdot t) \\ & + \sum_{j=1}^{\infty} \mathrm{Re}\left[V_{2j,\mathrm{as}} \right] \cdot e^{\alpha_{\mathrm{as}} \cdot z} \cdot \cos(-\beta_{\mathrm{as}} \cdot z - \omega \cdot t) \\ & - \sum_{j=1}^{\infty} \mathrm{Im}\left[V_{2j,\mathrm{as}} \right] \cdot e^{\alpha_{\mathrm{as}} \cdot z} \cdot \sin(-\beta_{\mathrm{as}} \cdot z - \omega \cdot t). \end{aligned} \tag{11}$$

Here, the initial value $V_{1,1} = V_0$ is the amplitude of the applied voltage. The voltage seen at position z $(0 \le z \le l_{\mathrm{as}})$ along the length of the

active section of the modulator by photons that enter the interaction region ($z = 0$) at $t = t_0$ can be written as [1]

$$\begin{aligned} V(z,t_0) = &\sum_{j=1}^{\infty} \mathrm{Re}\left[V_{2j-1,\mathrm{as}+1} \cdot e^{\alpha_{\mathrm{as}} \cdot l_{\mathrm{as}} - i \cdot \beta_{\mathrm{as}} \cdot l_{\mathrm{as}}}\right] \cdot e^{-\alpha_{\mathrm{as}} \cdot z} \\ &\cdot \cos(\delta \cdot z - \omega \cdot t_0) \\ &- \sum_{j=1}^{\infty} \mathrm{Im}\left[V_{2j-1,\mathrm{as}+1} \cdot e^{\alpha_{\mathrm{as}} \cdot l_{\mathrm{as}} - i \cdot \beta_{\mathrm{as}} \cdot l_{\mathrm{as}}}\right] \cdot e^{-\alpha_{\mathrm{as}} \cdot z} \\ &\cdot \sin(\delta \cdot z - \omega \cdot t_0) \\ &+ \sum_{j=1}^{\infty} \mathrm{Re}\left[V_{2j,\mathrm{as}}\right] \cdot e^{\alpha_{\mathrm{as}} \cdot z} \cdot \cos(-\delta' \cdot z - \omega \cdot t_0) \\ &- \sum_{j=1}^{\infty} \mathrm{Im}\left[V_{2j,\mathrm{as}}\right] \cdot e^{\alpha_{\mathrm{as}} \cdot z} \cdot \sin(-\delta' \cdot z - \omega \cdot t_0). \end{aligned} \tag{12}$$

where

$$\delta = \frac{2\pi \cdot f}{c} \cdot (n_{\mathrm{as}} - n_{\mathrm{opt}}) \tag{13}$$

and

$$\delta' = \frac{2\pi \cdot f}{c} \cdot (n_{\mathrm{as}} + n_{\mathrm{opt}}). \tag{14}$$

Here, n_{opt} is the effective index of the guided optical mode. Notice that for the case of a counter propagating optical signal, just the sign of n_{opt} has to be altered. The local change in the wave vector $\Delta\beta$ of the optical wave induced by the RF voltage applied to an electrooptic waveguide may be expressed as

$$\Delta\beta(z) = \Delta\beta_0 \cdot \frac{V(z,t_0)}{V_0} \tag{15}$$

where

$$\Delta\beta_0 = -\frac{\pi}{\lambda} \cdot n_{\mathrm{opt}}^3 \cdot r \cdot \frac{V_0}{w} \cdot \Gamma. \tag{16}$$

Here, λ is the free-space optical wavelength, r is the pertinent electrooptic coefficient, w is the inter-electrode gap, and Γ is the electrooptical overlap integral. The frequency-dependent electrooptically induced phase shift $\Delta\phi$ for photons incident at $t = t_0$ is then given by

$$\Delta\phi(f,t_0) = \int_0^{l_{\mathrm{as}}} \Delta\beta(z) \cdot dz. \tag{17}$$

We integrate the above expression and get

$$\begin{aligned} \Delta\phi(f,t_0) = \frac{\Delta\beta_0}{V_0} \cdot \Bigg[&\sum_{j=1}^{\infty} \mathrm{Re}\left[V_{2j-1,\mathrm{as}+1} \cdot e^{\alpha_{\mathrm{as}} \cdot l_{\mathrm{as}} - i \cdot \beta_{\mathrm{as}} \cdot l_{\mathrm{as}}}\right] \\ &\cdot \Big[f\alpha \cdot \cos(\omega \cdot t_0) + f\delta \cdot \sin(\omega \cdot t_0)\Big] \\ &- \sum_{j=1}^{\infty} \mathrm{Im}\left[V_{2j-1,\mathrm{as}+1} \cdot e^{\alpha_{\mathrm{as}} \cdot l_{\mathrm{as}} - i \cdot \beta_{\mathrm{as}} \cdot l_{\mathrm{as}}}\right] \\ &\cdot \Big[f\delta \cdot \cos(\omega \cdot t_0) - f\alpha \cdot \sin(\omega \cdot t_0)\Big] \\ &+ \sum_{j=1}^{\infty} \mathrm{Re}\left[V_{2j,\mathrm{as}}\right] \cdot \Big[b\alpha \cdot \cos(\omega \cdot t_0) \\ &\qquad + b\delta' \cdot \sin(\omega \cdot t_0)\Big] \\ &- \sum_{j=1}^{\infty} \mathrm{Im}\left[V_{2j,\mathrm{as}}\right] \\ &\cdot \Big[b\delta' \cdot \cos(\omega \cdot t_0) - b\alpha \cdot \sin(\omega \cdot t_0)\Big]\Bigg] \end{aligned} \tag{18}$$

where

$$f\alpha = \frac{1}{\alpha_{\mathrm{as}}^2 + \delta^2} \cdot \Big(\alpha_{\mathrm{as}} + \delta \cdot e^{-\alpha_{\mathrm{as}} \cdot l_{\mathrm{as}}} \cdot \sin(\delta \cdot l_{\mathrm{as}}) - \alpha_{\mathrm{as}} \cdot e^{-\alpha_{\mathrm{as}} \cdot l_{\mathrm{as}}} \cdot \cos(\delta \cdot l_{\mathrm{as}})\Big) \tag{19}$$

$$f\delta = \frac{1}{\alpha_{\mathrm{as}}^2 + \delta^2} \cdot \Big(\delta - \alpha_{\mathrm{as}} \cdot e^{-\alpha_{\mathrm{as}} \cdot l_{\mathrm{as}}} \cdot \sin(\delta \cdot l_{\mathrm{as}}) - \delta \cdot e^{-\alpha_{\mathrm{as}} \cdot l_{\mathrm{as}}} \cdot \cos(\delta \cdot l_{\mathrm{as}})\Big) \tag{20}$$

$$b\alpha = \frac{1}{\alpha_{\mathrm{as}}^2 + \delta'^2} \cdot \Big(-\alpha_{\mathrm{as}} + \delta' \cdot e^{\alpha_{\mathrm{as}} \cdot l_{\mathrm{as}}} \cdot \sin(\delta' \cdot l_{\mathrm{as}}) + \alpha_{\mathrm{as}} \cdot e^{\alpha_{\mathrm{as}} \cdot l_{\mathrm{as}}} \cdot \cos(\delta' \cdot l_{\mathrm{as}})\Big) \tag{21}$$

$$b\delta' = \frac{1}{\alpha_{\mathrm{as}}^2 + \delta'^2} \cdot \Big(-\delta' - \alpha_{\mathrm{as}} \cdot e^{\alpha_{\mathrm{as}} \cdot l_{\mathrm{as}}} \cdot \sin(\delta' \cdot l_{\mathrm{as}}) + \delta' \cdot e^{\alpha_{\mathrm{as}} \cdot l_{\mathrm{as}}} \cdot \cos(\delta' \cdot l_{\mathrm{as}})\Big). \tag{22}$$

By employing the identity

$$A \cdot \cos\phi + B \cdot \sin\phi = (A^2 + B^2)^{(1/2)} \cdot \sin\left[\tan^{-1}\left(\frac{A}{B}\right) + \phi\right] \tag{23}$$

we obtain both the amplitude and phase of the optical phase shift induced by the electrooptical microwave interaction

$$\begin{aligned} &\Delta\phi(f,t_0) \\ &= \frac{\Delta\beta_0}{V_0} \cdot \Bigg\{\Bigg[\sum_{j=1}^{\infty}\Big(f\alpha \cdot \mathrm{Re}\Big[V_{2j-1,\mathrm{as}+1} \cdot e^{\alpha_{\mathrm{as}} \cdot l_{\mathrm{as}} - i \cdot \beta_{\mathrm{as}} \cdot l_{\mathrm{as}}}\Big] \\ &\qquad - f\delta \cdot \mathrm{Im}\Big[V_{2j-1,\mathrm{as}+1} \cdot e^{\alpha_{\mathrm{as}} \cdot l_{\mathrm{as}}\, i - i \cdot \beta_{\mathrm{as}} \cdot l_{\mathrm{as}}}\Big] \\ &\qquad + b\alpha \cdot \mathrm{Re}[V_{2j,\mathrm{as}}] - b\delta' \cdot \mathrm{Im}[V_{2j,\mathrm{as}}]\Big)\Bigg]^2 \\ &\quad + \Bigg[\sum_{j=1}^{\infty}\Big(f\delta \cdot \mathrm{Re}\Big[V_{2j-1,\mathrm{as}+1} \cdot e^{\alpha_{\mathrm{as}} \cdot l_{\mathrm{as}} - i \cdot \beta_{\mathrm{as}} \cdot l_{\mathrm{as}}}\Big] \\ &\qquad + f\alpha \cdot \mathrm{Im}\Big[V_{2j-1,\mathrm{as}+1} \cdot e^{\alpha_{\mathrm{as}} \cdot l_{\mathrm{as}} - i \cdot \beta_{\mathrm{as}} \cdot l_{\mathrm{as}}}\Big] \\ &\qquad + b\delta' \cdot \mathrm{Re}[V_{2j,\mathrm{as}}] + b\alpha \cdot \mathrm{Im}[V_{2j,\mathrm{as}}]\Big)\Bigg]^2\Bigg\}^{1/2} \\ &\quad \cdot \sin\left[\tan^{-1}\left(\frac{A_0}{B_0}\right) + \omega \cdot t_0\right] \end{aligned} \tag{24}$$

with

$$\begin{aligned} A_0 = &\sum_{j=1}^{\infty} f\alpha \cdot \mathrm{Re}\Big[V_{2j-1,\mathrm{as}+1} \cdot e^{\alpha_{\mathrm{as}} \cdot l_{\mathrm{as}} - i \cdot \beta_{\mathrm{as}} \cdot l_{\mathrm{as}}}\Big] \\ &- f\delta \cdot \mathrm{Im}\Big[V_{2j-1,\mathrm{as}+1} \cdot e^{\alpha_{\mathrm{as}} \cdot l_{\mathrm{as}} - i \cdot \beta_{\mathrm{as}} \cdot l_{\mathrm{as}}}\Big] \\ &+ b\alpha \cdot \mathrm{Re}[V_{2j,\mathrm{as}}] - b\delta' \cdot \mathrm{Im}[V_{2j,\mathrm{as}}] \end{aligned} \tag{25}$$

$$\begin{aligned} B_0 = &\sum_{j=1}^{\infty} f\delta \cdot \mathrm{Re}\Big[V_{2j-1,\mathrm{as}+1} \cdot e^{\alpha_{\mathrm{as}} \cdot l_{\mathrm{as}} - i \cdot \beta_{\mathrm{as}} \cdot l_{\mathrm{as}}}\Big] \\ &+ f\alpha \cdot \mathrm{Im}\Big[V_{2j-1,\mathrm{as}+1} \cdot e^{\alpha_{\mathrm{as}} \cdot l_{\mathrm{as}} - i \cdot \beta_{\mathrm{as}} \cdot l_{\mathrm{as}}}\Big] \\ &+ b\delta' \cdot \mathrm{Re}[V_{2j,\mathrm{as}}] + b\alpha \cdot \mathrm{Im}[V_{2j,\mathrm{as}}]. \end{aligned} \tag{26}$$

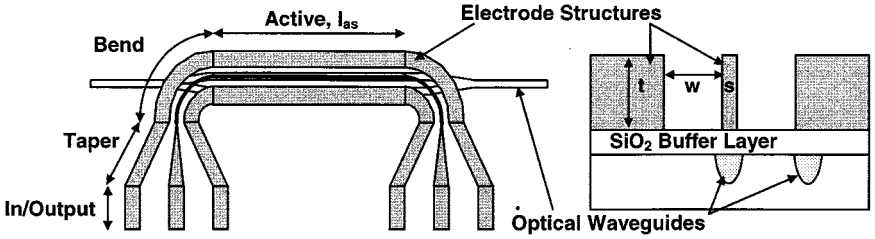

Fig. 2. Layout and cross section of coplanar TW thick electrode structure of the broad-band $LiNbO_3$ Mach–Zehnder interferometer modulator.

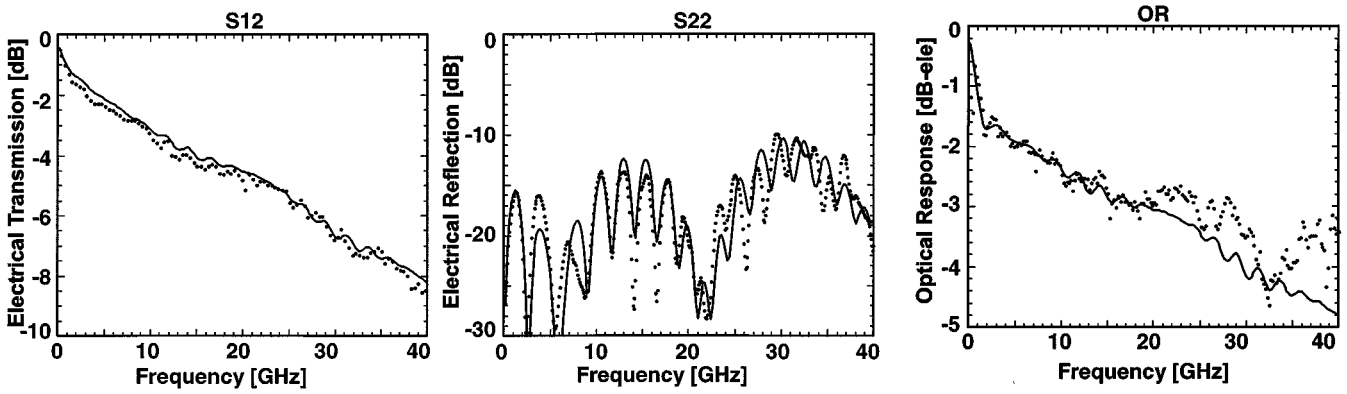

(a) (b) (c)

Fig. 3. Measured electrical and optical responses of the packaged modulator (dots) with the corresponding fit curves (solid).

Equation (24) is fully iterative and gives both the amplitude and phase of the optical phase shift induced by the optical microwave interaction. It can be programmed to compute, up to a chosen accuracy, the effects of any electric transmission-line configuration with multiple internal microwave reflections and absorption.

The expression for the optical phase shift as a function of frequency obtained above can be applied to a Mach–Zehnder interferometer with a push–pull electrode configuration. In this case, the optical output power is represented as [3]

$$P_{\text{out}} = T_d \cdot \frac{P_{\text{in}}}{2} \cdot \left[1 + \cos\left(\phi_0 + 2 \cdot \Delta\phi(f, t_0)\right)\right] \tag{27}$$

where ϕ_0 is the dc bias, P_{in} is the optical input power, and T_d is the overall optical losses. For quadrature bias ($\phi_0 = 90^\circ$) and under small-signal operation, the above expression becomes

$$P_{\text{out}} = T_d \cdot \frac{P_{\text{in}}}{2} \cdot \left[1 - 2 \cdot \Delta\phi(f, t_0)\right]. \tag{28}$$

From the above, the magnitude of the normalized optical frequency response in decibel electrical is

$$\text{OR}(f) = 20 \cdot \log \frac{\left|\Delta\phi(f, t_0)\right|}{\Delta\phi(0, t_0)}. \tag{29}$$

III. Broad-Band $LiNbO_3$ TW Optical-Intensity Modulator

The model developed here was applied to study the performance of a fully packaged broad-band modulator designed for operation at 1.3 μm and fabricated on a z-cut $LiNbO_3$ wafer. The potential for broad-band operation of these devices is limited by velocity mismatch of the electrical and optical signal, by losses intrinsic to the device electrode, and by impedance mismatch between the device and the 50-Ω driver or between different segments on the electrode. To overcome these problems, we employed a thick coplanar electrode structure as described in [4]. The layout of the device is shown in Fig. 2. We used a Mach–Zehnder interferometer modulator with a thick coplanar electrode structure, as presented in [5]. Gold electrode thickness (t) was 27 μm on an $LiNbO_3$ substrate coated with 0.9-μm SiO_2 buffer layer. Active strip electrode width (s) is 8 μm, its gap to the ground planes (w) is 25 μm, and its interaction length (l_{as}) is 24 mm. Due to packaging requirements, the electrical transmission line integrated on the $LiNbO_3$ modulator is composed of the following sections (see Fig. 2):

1) input/output section;
2) tapers;
3) bends;
4) active section

Microwave input/output to the device is applied through coaxial microwave V connectors to the input/output section, with dimensions properly matching the connectors. The tapers were designed to provide dimensional matches between input/output and active sections of the modulator, and the bends are necessary to locate optical and electrical access ports at different edges of the $LiNbO_3$ substrate. Using an HP8722D network analyzer, the electrical and optical responses of the fully packaged modulator were measured over a 50-MHz–40-GHz span. For the optical response, an NEL broad-band internally unterminated waveguide detector was used, without correction for the detector response. Additional information on design and measurement results is given in [5].

To fit our measurements, we employed a nine-section model ($N = 7$) including 50-Ω input/output line ($Z_0 = Z_{N+1} = 50\ \Omega$), input/output transition, input/output taper, input/output bend, and the active section (see Fig. 2). This results in four kinds of sections with different impedances Z_i, absorptions α_i, and microwave indexes n_i so that a 12-fit-parameter calculation has to be solved. The initial values used were: 1) electrical time-domain reflection (TDR) measurements for the impedances Z_i; 2) individual section measurements similar to those described in [3] for the losses α_i; and 3) design values for the effective indexes n_i. The lengths l_i were given by the layout of our electrode structure. In the second step, the losses were fitted to

TABLE I
MODEL PARAMETERS USED TO CALCULATE THE FIT CURVES OF FIG. 3

Section:	l_i [mm]	Z_i [Ω]	α_i [(cm√GHz)$^{-1}$]; [(cmGHz^3)$^{-1}$]	n_i
transition	0.4	40	0.010; 2.0 ·10^{-6}	3.6
taper	2.4	49	0.010; 2.0 ·10^{-6}	3.3
bend	0.2	42	0.042; 1.3 ·10^{-6}	2.5
active	24.0	41	0.042; 1.3 ·10^{-6}	2.138

match the electrical transmission (S_{21}) measurements. It has been found that the best match could be obtained by choosing a square root and cubic frequency-dependent loss term. Due to the short length of the transition, taper, and bend sections, the value of their loss term has limited accuracy, and should be measured individually. In the third step, the impedances were changed such that the amplitudes of the response for the electrical reflection measurement (S_{22}) were obtained.

In the final step, the microwave index of the active section was chosen such that the slope of the optical response at high frequency is obtained. Also, the other indexes have been adjusted so that the response of the electrical reflection is matched. It has been found that the electrical microwave index in the active section closely matches the optical one $(n_{\rm opt} = 2.138)$. The final curve fit results of (7), (8), and (29), together with the measurements, are shown in Fig. 3. The relative optical response has been adjusted to the 3-GHz point of the fit curve, thereby neglecting any acoustic resonance or other low-frequency effects, as observed in [5]. As shown, there is a good agreement between model and measurements, considering variations of the optical detector response at frequencies higher than 20 GHz. The final fit parameters are summarized in Table I. As we use here a nine-section model, the results are slightly different than the ones obtained in [5] for a five-section model.

IV. CONCLUSION

We have given an iterative model for the reflected and transmitted electrical response, as well as the amplitude and phase of the optical response of a general multisectional TW optical intensity modulator. These expressions are very helpful for the analysis of existing devices, and they should be useful in future device design.

REFERENCES

[1] R. C. Alferness, S. K. Korotky, and E. A. Marcatili, "Velocity-matching techniques for integrated optic traveling wave switch/modulators," *IEEE J. Quantum Electron.*, vol. QE-20, pp. 301–309, Mar. 1984.

[2] W. K. Burns, "Analytic output expression for integrated optic phase reversal modulators with microwave loss," *Appl. Opt.*, vol. 28, no. 15, pp. 3280–3283, 1989.

[3] G. K. Gopalakrishnan, W. K. Burns, R. W. McElhanon, C. H. Bulmer, and A. S. Greenblatt, "Performance and modeling of broad-band $LiNbO_3$ traveling wave optical intensity modulators," *J. Lightwave Technol.*, vol. 12, pp. 1807–1819, Oct. 1994.

[4] ——, "40 GHz, low half-wave voltage Ti: $LiNbO_3$ intensity modulator," *Electron. Lett.*, vol. 28, no. 9, pp. 826–827, 1992.

[5] W. K. Burns, M. M. Howerton, R. P. Moeller, R. Krähenbühl, R. W. McElhanon, and A. S. Greenblatt, "Low drive voltage, broad-band $LiNbO_3$ modulators with and without etched ridges," *J. Lightwave Technol.*, vol. 17, pp. 2551–2555, Dec. 1999.

Field Expressions and Patterns in Elliptical Waveguide

Sen Li and Bai-Suo Wang

***Abstract*—The elliptic waveguide have been used in several systems such as satellite communication and radar feed lines. In this paper, the field expressions in Fourier series are obtained. The field patterns with over 30 modes with three eccentricities ($e = 0.3, 0.75, 0.9$) are plotted.**

***Index Terms*—Elliptical waveguide, field patterns.**

In 1938, Chu first studied the transmission of an electromagnetic wave in an elliptic guide [1]. His classic field plots are used in many standard text and reference books, where the field pattern of the ${}_cE_{01}$ is incorrect. The field expressions and plots in elliptic waveguide have since been studied by many researchers [2]–[5].

However, some of those patterns are with sketches, while others are only for the first six or eight modes.

In many applications, the plots for higher order modes are interesting. In this paper, the field expressions are discussed by means of expanding the Mathieu function into the Fourier series [6]. The field patterns with complete electromagnetic lines are plotted. The density of the field lines is proportional to the field strength.

The major and minor axes of the ellipse are $2a$ and $2b$, respectively. Three kinds of guide sizes, corresponding to $e = 0.3, 0.75, 0.9$ are a $\times b = 10 \times 9.539392$ cm^2, 10×6.614378 cm^2, and 10×4.358899 cm^2, respectively. The coefficients A and B in the Fourier expression of the Mathieu functions ce_m, se_m, and the involved parameters are calculated. Take ${}_cH_{11}$ with $e = 0.75$ e.g., $A_1 = 9.9790E-1$, $A_3 = -6.4770E-2$, $A_5 = 1.3454E-3$, $A_7 = -1.3836E-5$, $A_9 = 8.5050E-8$, $A_{11} = -3.4785E-10$, $A_{13} = 1.0151E-12$, $A_{15} = -2.2201E-15$, $A_{17} = 3.7750E-18$, $A_{19} = -5.1333E-21$, and $f_c = 8.8967E-1$ GHz.

The field patterns are shown in Figs. 1–3. Two digits below each mode sign represent its eigenmode number. The eigenmode numbers beyond 100 are not written.

Manuscript received February 25, 1999.

The authors are with the Information Engineering College, Dalian Maritime University, Dalian 116026, China.

Publisher Item Identifier S 0018-9480(00)03756-X.

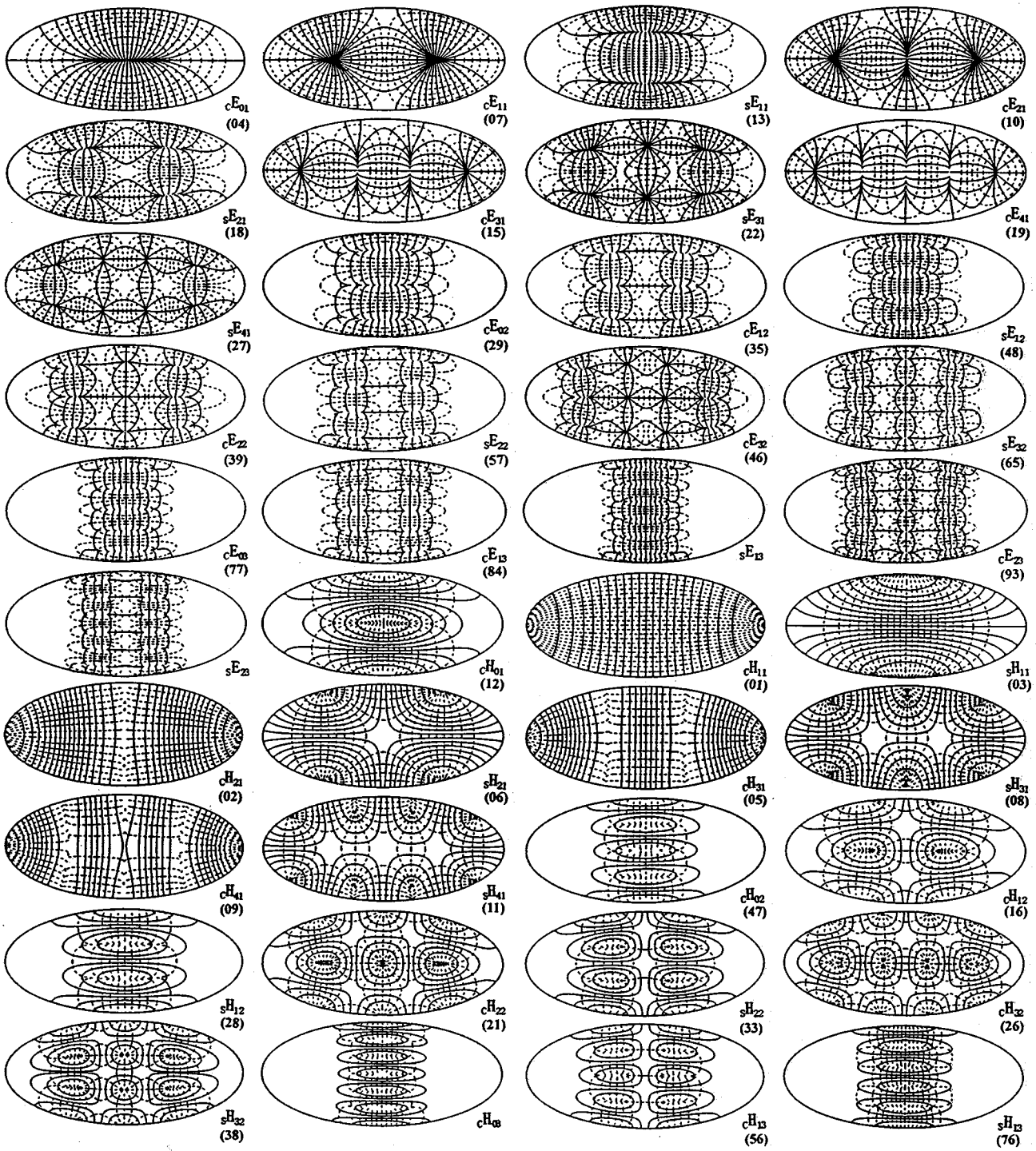

Fig. 1. Field patterns $e = 0.30$ (—E: lines, - - - H lines).

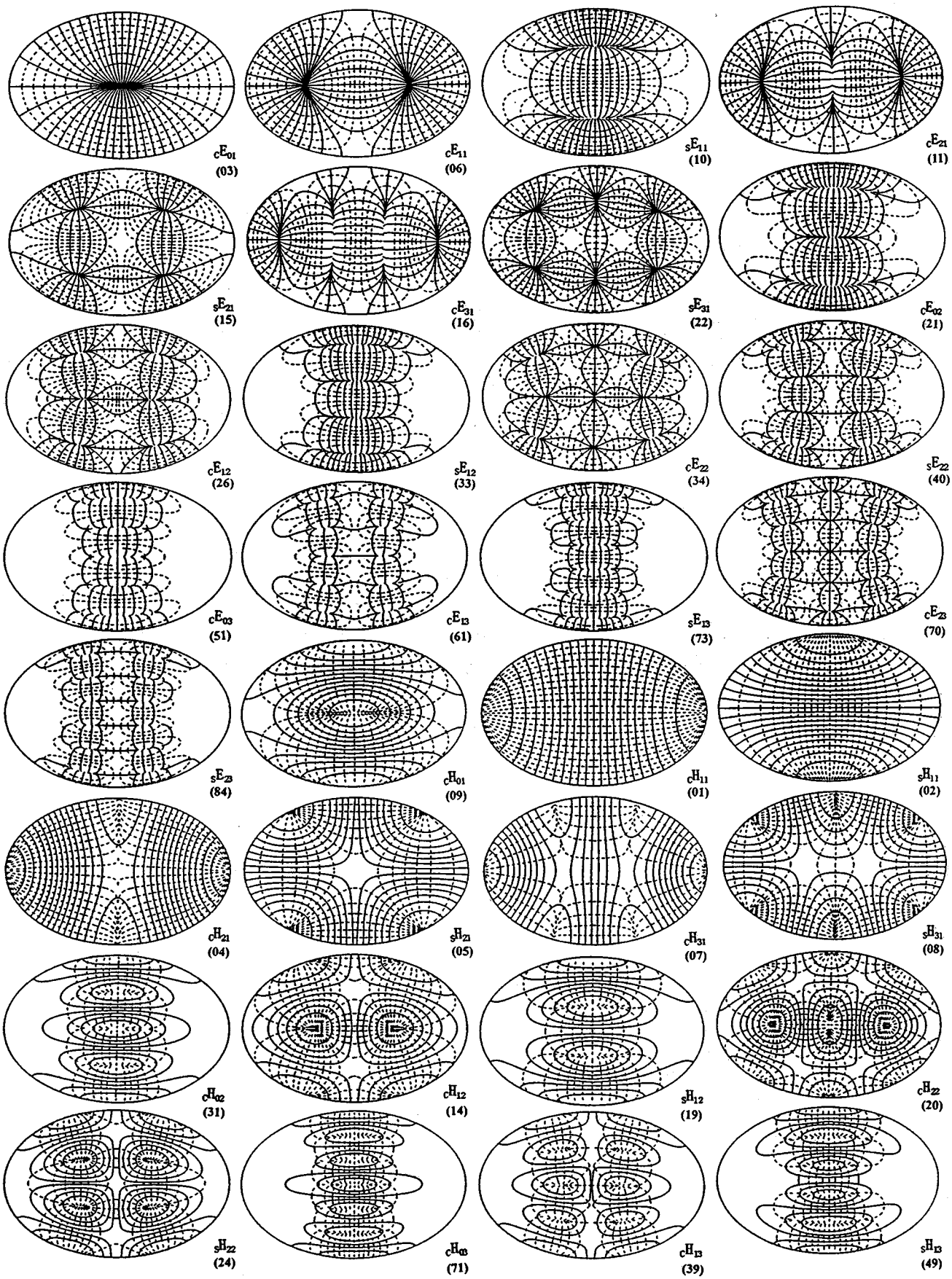

Fig. 2. Field patterns $e = 0.75$ (—E: lines, - - - H lines).

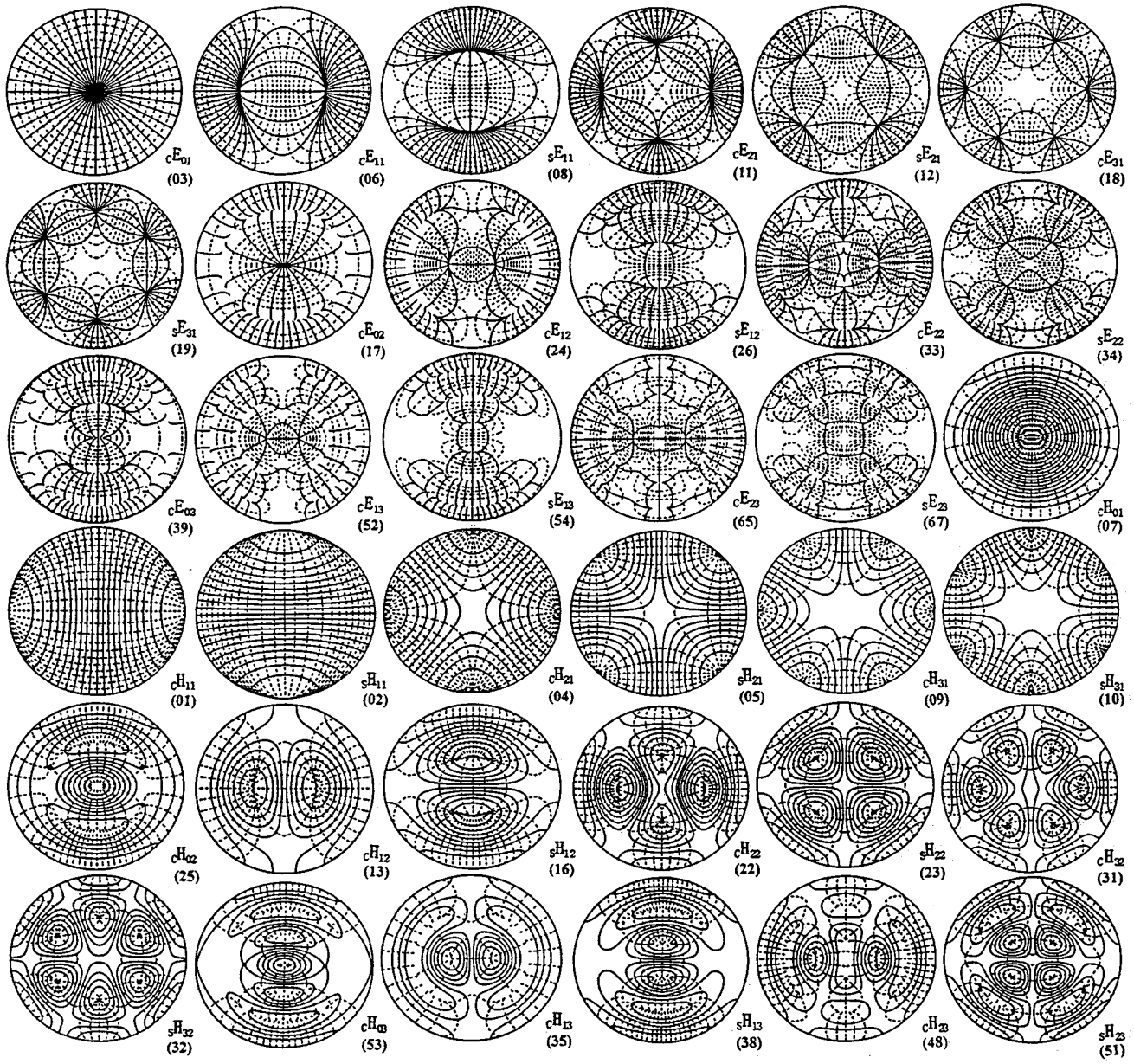

Fig. 3. Field patterns $e = 0.90$ (—E: lines, - - - H lines).

ACKNOWLEDGMENT

The authors are very grateful to Prof. S.-J. Zhang for his help and support in performing this work.

REFERENCES

[1] L. J. Chu, "Electromagnetic waves in elliptic hollow pipes of metal," *J. Apply Phys.*, vol. 9, pp. 583–591, Sept. 1938.

[2] G. Piefke, "Die übertagungseigenschaften des elliptischen hohleithers," *Arch. Elektr. Üebertrag.*, vol. 18, pp. 255–267, Apr. 1964.

[3] J. G. Kretzschmar, "Wave propagation in hollow conducting elliptical waveguides," *IEEE Trans. Microwave Theory Tech.*, vol. MTT-18, pp. 547–554, Sept. 1970.

[4] B.-S. Wang and Z.-J. Li, "Field plots in elliptic waveguide," in *Proc. 3rd Int. Antennas EM Theory Symp.*, Najing, China, 1993, pp. 351–318.

[5] B. H. Wang, K. Y. Lam, M. S. Leong, and P. S. Kooi, "Elliptical waveguide analysis using improved polynomial approximation," *Proc. Inst. Elect. Eng.*, pt. H, vol. 141, no. 6, pp. 483–488, Dec. 1994.

[6] N. W. McLachalan, *Theory and Application of Mathieu Functions*. Oxford, U.K.: Clarendon, 1947, ch. 2, 3, 9, 18.

[7] F. A. Alhargan and S. R. Judah, "Tables of normalized cutoff wavenumbers of elliptic cross-section resonators," *IEEE Trans. Microwave Theory Tech.*, vol. 42, pp. 333–338, Feb. 1994.

[8] C. S. Lee, S. W. Lee, and S. L. Chang, "Plot of modal field distribution in rectangular and circular waveguide," *IEEE Trans. Microwave Theory Tech.*, vol. MTT-33, pp. 271–274, Mar. 1985.

A Power and Efficiency Measurement Technique for Active Patch Antennas

Elmahdi A. Elkhazmi, Neil J. McEwan, and Nazar T. Ali

***Abstract*—In this paper, the power input to the radiating element of an active microstrip patch antenna is measured using a small sensing patch, which is weakly coupled to a radiating edge. Combined with an estimate of patch radiation efficiency, this also yields a measurement of total radiated power. The method has advantages of convenience, insensitivity to room reflections, and a weakly frequency-dependent calibration factor.**

***Index Terms*—Active antennas, antenna measurements, microstrip antennas.**

I. Introduction

Many papers have described active patch antennas for transmitting applications. These antennas may be defined as an active device very closely integrated with a passive radiating structure (referred to here as the *radiator*), and with little or no intervening circuitry [1]. They fall into the general classes of self-oscillating antennas and radiating power amplifiers. The first group may be further divided into those using a one-port radiator coupled to a negative resistance circuit or device, and designs using a two-port radiator achieving oscillation via a feedback path. Performance assessment requires a measurement of the total power radiated into space, and of the conversion efficiency relating this power to the dc input power. For the class of radiating power amplifiers, either power-added efficiency (PAE) or overall efficiency may also be used as figures of merit [2].

II. Existing Methods

Most papers have described measurement of the power output of an active antenna by coupling it to a receiving antenna of known gain under far-field conditions (e.g., [3]). The Friis equation may be used and an estimate for the gain of the radiator under test must be inserted. If not easily calculable, this could be measured conventionally by comparison with a reference antenna, using either an identical copy of the radiator without active devices or the actual radiator in a passive mode by disconnecting it from the active device and reconnecting at the same point to a separate feed line.

For the class of radiating power amplifiers, An *et al.* [4] describe how an identical radiator can be used in a substitution method to measure the transducer gain of the power amplifier (minus radiator) without the need to disconnect it. The substitution removes the need to calculate the Friis coupling factor, and the associated uncertainties. Another form of substitution technique [5], [6] used a substituted passive copy to measure total power output. In [5], a correction factor $1/(1-|\Gamma|^2)$, based on a network analyzer measurement of the input reflection coefficient of the passive copy, was included, as it had also been in [4]. If disconnection is permitted, these substitutions can use the actual radiator rather than a copy. In [4], an anechoic environment was assumed. We note that this could be relaxed somewhat if care is taken to keep all scatterers stationary and to put the substituted antenna in exactly the same place as the active one. This approach was used in [5].

The point has been somewhat neglected that all these techniques, including the basic Friis equation method, strictly measure the *input* power accepted by the radiator at its feed point(s), rather than the total power radiated into space. However, this enables the amplifier and radiator contributions to overall efficiency to be clearly separated.

Manuscript received May 14, 1999.

The authors are with the Department of Electronic and Electrical Engineering, University of Bradford, West Yorkshire BD7 1DP, U.K.

Publisher Item Identifier S 0018-9480(00)03757-1.

III. An Alternative Technique

An alternative method now described is to provide the active patch radiator with a small sensing patch, which is mounted on the same board as the main patch antenna and placed close to one of its radiating edges. The sensing patch is connected to an output coaxial connector. The connection can be made via a coaxial probe from the ground-plane side of the board, or via a microstrip line taken from the sensing patch. The sensor and coupling factor are kept small to ensure negligible perturbation of the main antenna.

Fig. 1 shows how this was implemented for a particular radiating power amplifier. The active antenna shown is similar to that described in [3] and is an experimental version with a one-wavelength line interposed between the patch and power transistor. (The line was included to facilitate separate current/voltage waveform measurements, and might be omitted in an operational version, or possibly replaced by a quarter-wavelength line to approximate a class-F harmonic termination, as in [6].)

The high coupling reactance (about 1.4 kΩ) between the main and sensing patches implies that the latter approximates to a constant current source feeding into its own capacitance to ground. A 50-Ω coaxial load to ground was, therefore, included as shown to improve the match at port 2 and reduce errors arising from connecting an imperfectly matched power meter or spectrum analyzer at that point. The ground capacitance of the sensing patch was arranged as the first element of a filter designed to have a very flat response over the small band of frequencies at which the antenna might be operated. The simplest filter could have one additional series or shunt inductor; the example shown used three extra components, forming a low-pass ladder network and providing adequate rejection of harmonic outputs when measuring with a thermistor power meter. If the 50-Ω load is unscrewed to form a temporary port 3, correct filter response can be verified by measuring S_{23}.

To calibrate the sensor, the main microstrip line was cut near its center to disconnect the transistor, and the section feeding the patch was reconnected to a temporary coaxial probe (port 1) fitted at this point. The radiator and sensor now become a passive two-port. The necessary calibration factor relates the sensor's output power to the power accepted by the radiator from the power amplifier, and is

$$\left|S'_{21}\right|^2 = \frac{|S_{21}|^2}{\left(1-|S_{11}|^2\right)}. \tag{1}$$

IV. Results

In the layout shown, the sensing patch was empirically trimmed to give inter-port coupling of about -25 dB near the resonant frequency of the patch. The board was then measured carefully on a well-calibrated network analyzer (HP 8510C), avoiding room reflections as far as possible. Fig. 2 shows the resulting plot of $|S'_{21}|^2$. In order to show the inherent frequency dependence of the sensor, this plot has been taken with the three added elements of the output filter omitted. Also shown in this plot is the return loss of the main patch; it can be seen that this is negligibly affected by the presence of the sensing patch. The plot has good accuracy where the return loss is better than about -0.5 dB, this being considered necessary for (1) not to be too sensitive to errors in measuring this quantity.

The interesting result is that $|S'_{21}|^2$ has a quite slowly varying magnitude over a much wider band than the resonant bandwidth of the patch.

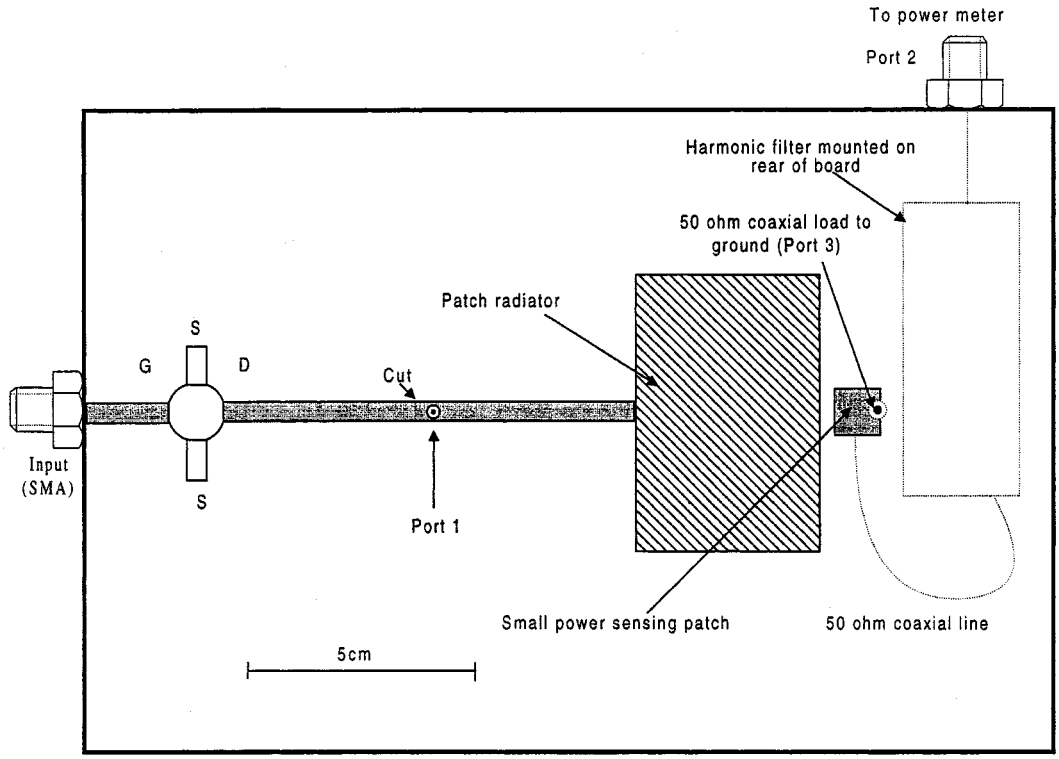

Fig. 1. Test layout for power and efficiency measurements (board thickness: 1.65 mm, $\varepsilon_r = 2.55$, transistor type: Fujitsu FLL351ME).

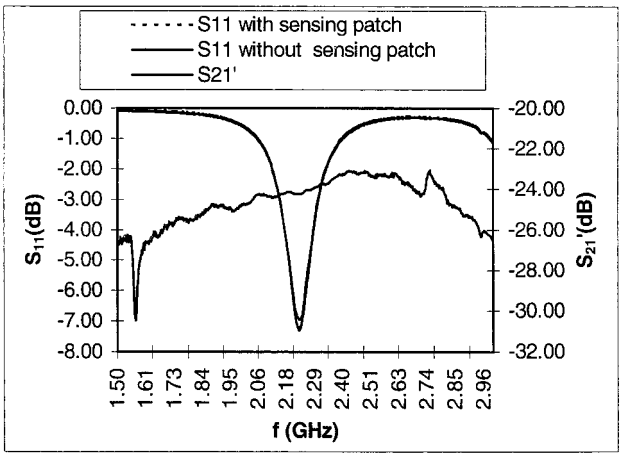

Fig. 2. Calibration factor of the sensing patch (without filter).

The patch impedance varies widely over this band, which indicates that the correction for impedance variation is working accurately. The graph shows small residual frequency dependence on a finer frequency scale than would be expected from the patch structures alone, and it has been considered legitimate to smooth it slightly. The variations were attributed to random network analyzer errors, minor room reflections, and standing waves on the outer surfaces of the network analyzer test cables. For measurements between 2.2–2.5 GHz, the smoothed calibration curve is believed to be accurate to within ± 0.2 dB. This is probably a better accuracy than could easily be achieved by coupling to a separate antenna. For most transistors, the operating point would be selected between 2.15–2.35 GHz, over which range the total variation of the calibration factor is only 0.4 dB.

The best PAE of the power amplifier was measured by this method as 49.3% at 2.36 GHz with the patch accepting 1.29 W from the transistor. The RF input power to the amplifier was obtained as the difference of incident (532 mW) and reflected (190 mW) powers measured using a directional coupler, and without gate matching. Drain bias was 6 V and drain current 320 mA with quiescent bias at pinchoff. The measured efficiency is in good agreement with the figure of 48% quoted in [3].

In measurements taken conventionally by coupling to a second antenna, fine scale frequency dependence of the calibration can be created by extraneous scatterers unless the environment has good anechoic properties. If, however, the spacing is reduced to make the direct path dominant, frequency dependence arises instead from multiple reflections between the two antennas. The new method was found to be very convenient in avoiding these effects and in making it easy to optimize the operating frequency.

V. Sensor Frequency Dependence

A simple explanation of the weakly frequency-dependent calibration factor of the sensing patch is offered by the equivalent circuit shown in Fig. 3, which would be valid for frequencies near resonance where the main patch fields can be approximated as pure TM_{10} mode. The sensing patch is capacitively coupled to the radiating edge of the main radiator, which has been represented as a low impedance transmission line with end radiation conductances G_1, G_2. The coupling reactance greatly dominates the 25-Ω impedance level of the parallel internal and external loads. The sensor, therefore, outputs a power proportional to $\omega^2|V_2|^2/(1+\omega^2\tau^2)$, where V_2 is the edge voltage of the patch and time constant τ is the product of 25 Ω and the ground capacitance C_G(here, about 1.5 pF) of the sensing patch. The numerator dependence is the dominant one in this case. The equivalent source model of the main patch attributes most of its radiation to magnetic current sources, principally at the radiating edges, with intensities proportional to V_1 and V_2. An isolated magnetic Hertzian dipole of fixed intensity radiates a total power proportional to ω^2. This was found to be roughly true for single finite length slots, so these ω^2 dependencies will cancel in the

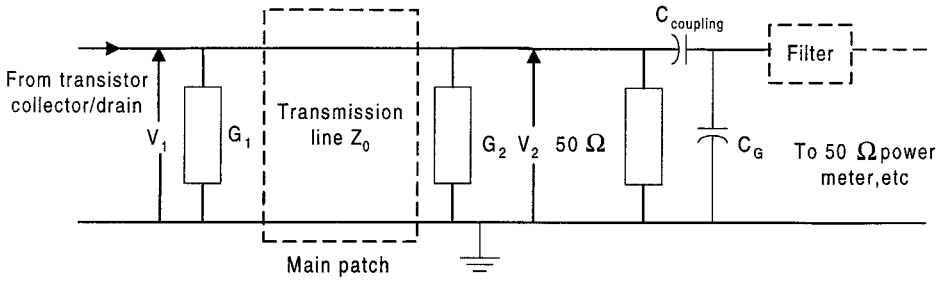

Fig. 3. Simple equivalent circuit of main patch and power sensor.

expression for $|S'_{21}|^2$. The other principal frequency dependencies in the system are the relationship between the edge voltages V_1 and V_2, and the radiating array factor of the two slots that affects the total power radiated. Unlike the input return loss of the patch, none of these factors determining $|S'_{21}|^2$ exhibits a strongly resonant behavior.

VI. Conclusion

In this paper, a new method was described for performance assessment of an active patch antenna. It should be applicable to any active antenna with a one-port patch radiator, whether self-oscillating or otherwise. Interesting features of this method are that it eliminates the uncertainties involving in using the standard Friis equation method, or the substitution method, and largely eliminates error introduced by an imperfect anechoic environment. The method can be used with good accuracy in an open laboratory, without anechoic walls, provided reasonable care is taken to avoid strong reflections from nearby obstacles. Another interesting feature is that a nearly frequency-independent calibration constant can be obtained over a wider band than the resonant bandwidth of the patch radiator under test. If desired, a very low-order filter can be fitted to the sensor to remove the already small frequency dependence, and this is very convenient when adjusting the operating conditions such as frequency, drive level, and bias to optimize the output power or the efficiency.

Like the existing methods of power measurement, the technique described measures power input to the radiating structure, and an estimate or measurement of radiation efficiency (e.g., [7], [8]) should be incorporated to find the true total radiated power.

References

[1] Y. Qian and T. Itoh, "Progress in active integrated antennas and their applications," *IEEE Trans. Microwave Theory Tech.*, vol. 46, pp. 1891–1900, Nov. 1998.

[2] N. O. Sokal and I. Novak, "Classes of RF power amplifiers A through S, how they operate, and when to use them," in *IEEE Electron. Conf.*, Boston, MA, June 1995, pp. 337–400.

[3] V. Radisic, S. T. Chew, Y. Qian, and T. Itoh, "High-efficiency power amplifier integrated with antenna," *IEEE Microwave Guided Wave Lett.*, vol. 7, pp. 39–41, Feb. 1997.

[4] H. An, B. Nauwelaers, and A. Van de Capelle, "Measurement technique for an active microstrip antennas," *Electron. Lett.*, vol. 29, no. 18, pp. 1646–1647, Sept. 1993.

[5] E. Elkhazmi, N. J. McEwan, and J. Moustafa, "Control of harmonic radiation from an active microstrip antenna," *J. Int. Nice Antennas*, pp. 313–316, Nov. 1996.

[6] V. Radisic, Y. Qian, and T. Itoh, "Novel architectures for high-efficiency amplifiers for wireless applications," *IEEE Trans. Microwave Theory Tech.*, vol. 46, pp. 1901–1909, Nov. 1998.

[7] D. M. Pozar and B. Kaufman, "Comparison of three methods for the measurement of printed antenna efficiency," *IEEE Trans. Antenna Propagat.*, vol. 36, pp. 136–139, Jan. 1988.

[8] R. H. Johnston and J. G. McRory, "An improved small antenna radiation-efficiency measurement method," *IEEE Antenna Propagat. Mag.*, vol. 40, pp. 40–47, Oct. 1988.

On the Goubau–Schwering Beam Waveguide Using a Modified Paraxial Approximation

Karl E. Lonngren

***Abstract*—In this paper, we demonstrate that the beam waveguide can be easily postulated by using a modified version of the paraxial approximation.**

***Index Terms*—Beam waveguide, paraxial approximation.**

The *paraxial approximation* is a technique that is gaining currency in solving diffraction problems in electromagnetic theory. In particular, it is found that in Cartesian coordinates, the far field is the two-dimensional Fourier transform of the field within the aperture. It is described in recent literature [1]. The purpose of this paper is to extend the paraxial approximation and demonstrate that the electromagnetic fields in the beam waveguide described originally by Goubau and Schwering [2], [3] can be directly obtained.

Goubau and Schwering calculated the transverse distribution of the electromagnetic fields that could propagate and be guided by a structure consisting of periodically displaced lenses. They found that the transverse distribution would be expressed in terms of modes that consisted of a Gaussian times a Laguerre polynomial in cylindrical coordinates [2] and a Gaussian times a Hermite polynomial in Cartesian coordinates [3]. This mode structure was experimentally confirmed at microwave frequencies [4], [5]. Additional results can be found in [6]–[8].

With reference to Fig. 1(a), and in the spirit of the paraxial approximation [1], the far field $E(x, y, z)$ is written as

$$E(x,y,z) = \frac{j}{\lambda}\int_{S'} \frac{E(x',y',z')e^{-j\beta r''}}{r''}dx'\,dy' \tag{1}$$

where the single prime indicates the coordinates of the aperture. The distance r'' is the distance between an element within the aperture and the far-field point, and is expressed as

$$r'' = \sqrt{(x-x')^2 + (y-y')^2 + (z-z')^2}. \tag{2}$$

Manuscript received July 14, 1999.

The author is with the Department of Electrical and Computer Engineering, The University of Iowa, Iowa City, IA 52242 USA.

Publisher Item Identifier S 0018-9480(00)03758-3.

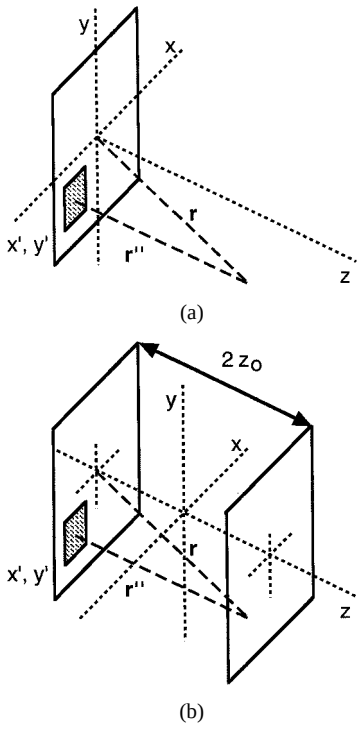

Fig. 1. Plane-wave element as part of a plane aperture. (a) Plane at $z = 0$. (b) Planes at $z = \pm z_o$.

In the standard paraxial approximation for diffraction [1], one approximates r'' with

$$r'' \sim r = \sqrt{x^2 + y^2 + z^2} \tag{3}$$

in the amplitude terms and uses the binomial expansion

$$r'' \sim r - \frac{xx' + yy'}{r} \tag{4}$$

in the phase terms. The aperture is located at $z' = 0$. In addition, the terms containing

$$\frac{(x')^2}{r} \quad \text{and} \quad \frac{(y')^2}{r}$$

and higher order are neglected, as they are considered to make an insignificant contribution.

In our *modified paraxial approximation* with the beam waveguide application in mind, we do expect and will require that the wave propagation be predominantly in the z direction, as shown in Fig. 1(b). We approximate r'' with

$$r'' \sim 2z_o \tag{5}$$

in the amplitude terms and expand (2) with the binomial expansion

$$r'' \sim 2z_o - \frac{xx' + yy'}{2z_o} + \frac{x'^2 + y'^2}{4z_o} + \frac{x^2 + y^2}{4z_o} \tag{6}$$

in the phase terms. The aperture is located at $z' = -z_o$. We retain the higher order terms. After substituting (5) and (6) in (1), we obtain

$$E(x, y, +z_o) = \frac{j}{\lambda 2 z_o} \int_{S'} E(x', y', -z_o) \times e^{-j\beta\left(2z_o - \frac{xx' + yy'}{2z_o} + \frac{x'^2 + y'^2}{4z_o} + \frac{x^2 + y^2}{4z_o}\right)} dx'\, dy' \tag{7}$$

or

$$E(x, y, +z_o) e^{j\beta\left(\frac{x^2 + y^2}{4z_o}\right)} = \frac{j e^{-j\beta 2z_o}}{\lambda 2 z_o} \int_{S'} E(x', y', -z_o) \times e^{-j\beta\left(\frac{xx' + yy'}{2z_o} + \frac{x'^2 + y'^2}{4z_o}\right)} dx'\, dy'. \tag{8}$$

In (8), the two quadratic exponential terms can be removed with *phase correcting lenses* at both locations. The term in front of the integral sign is the normal wave propagation for a distance $2z_o$. After removing these terms, we obtain

$$E(x, y, +z_o) = \int_{S'} E(x', y', -z_o) e^{-j\beta\left(\frac{xx' + yy'}{2z_o}\right)} dx'\, dy'. \tag{9}$$

Equation (9) is the result that we seek in that the field at $z = +z_o$ is the Fourier transform of the field at $z = -z_o$ if the aperture were infinite in extent. A Gaussian times a Hermite polynomial satisfies this in Cartesian coordinates, which is the normal mode [3]. Equation (9) can be transformed to cylindrical coordinates [1] with the result that a Gaussian times a Laguerre polynomial is the Hankel transform of itself and, thus, is a mode in cylindrical coordinates [2].

ACKNOWLEDGMENT

The author wishes to acknowledge his former colleagues and teachers G. Goubau, F. Schwering, J. B. Beyer, E. H. Scheibe, and J. W. Mink for discussions concerning the beam waveguide, and A. Korpel and E.-W. Bai for discussions concerning the paraxial approximation.

REFERENCES

[1] S. Ramo, J. Whinnery, and T. Van Duzer, *Fields and Waves in Communication Electronics*. New York: Wiley, 1994, pp. 618–624.
[2] G. Goubau and F. Schwering, "On the guided propagation of electromagnetic wave beams," *IRE Trans. Antennas Propagat.*, vol. AP-9, pp. 248–256, May 1961.
[3] F. Schwering, "Reiterative wave beams of rectangular symmetry," *Arch. Elektr. Uebertrag.*, vol. 15, pp. 555–564, 1961.
[4] J. B. Beyer and E. H. Scheibe, "Loss measurements of the beam waveguide," *IEEE Trans. Microwave Theory Tech.*, vol. MTT-11, pp. 18–22, Jan. 1963.
[5] J. W. Mink and E. H. Scheibe, "A dual-mode beam waveguide resonator and frequency stabilizer at millimeter—wave frequencies," *IEEE Trans. Microwave Theory Tech.*, vol. MTT-14, pp. 222–228, May 1966.
[6] G. Goubau, "Beam waveguides," in *Advances in Microwaves*. New York: Academic, 1968, vol. 3.
[7] P. F. Goldsmith, "Quasioptical techniques at millimeter and submillimeter wavelengths," in *Infrared and Millimeter Waves*, K. J. Button, Ed. New York: Academic, 1983, vol. 6.
[8] J. W. Mink and F. Schwering, "Hybrid dielectric slab–beam waveguide for the sub-millimeter wave region," *IEEE Trans. Microwave Theory Tech.*, vol. 41, pp. 1720–1729, Oct. 1993.

A Low-Impedance Coplanar Waveguide Using an $SrTiO_3$ Thin Film for GaAs Power MMIC's

Mitsuru Tanabe, Mitsuru Nishitsuji, Yoshiharu Anda, and Yorito Ota

***Abstract*—A novel structure for coplanar-waveguide transmission lines with low impedance and low loss is demonstrated in this paper. The new structure simply has a high dielectric $SrTiO_3$ thin film underneath the coplanar conductors. Due to the high dielectric constant of $SrTiO_3$, the coplanar line exhibited characteristic impedance as low as 18 Ω with a slot width of 5 μm and the center conductor width of 50 μm, while a conventional coplanar line on GaAs showed only 30 Ω with the same configuration. The newly developed coplanar structure is easily applicable for present GaAs monolithic-microwave integrated-circuit (MMIC) technology, especially for power MMIC's and low-impedance devices.**

***Index Terms*—Coplanar waveguides, impedance transfomers, MMIC's, SrTiO.**

I. Introduction

Coplanar waveguide (CPW) transmission lines have several advantages such as low dispersion, low coupling between adjacent lines, and low fabrication cost. In spite of these superior features, CPW's have not been utilized extensively thus far because of a lack of appropriate design tools with basic coplanar elements. Recently, however, demands for low-cost GaAs monolithic microwave integrated circuits (MMIC's) have been expanding into the millimeter-wave band in order to realize commercial systems, such as local multipoint distribution system (LMDS), satellite communication systems, and collision warning radar system. Thus, the interest in coplanar-line circuits has increased steadily [1].

Low-impedance transmission lines are used as impedance transformers of input matching networks for low-impedance devices such as power field-effect transistors (FET's) or photodiodes. For example, large-periphery GaAs FET's with the total gatewidth of over several hundreds micrometers have input impedance of only several ohms. In order to transform the impedance into the usual 50 Ω, the transmission lines must have characteristic impedance of, at most, 20 Ω. Conventional CPW's fabricate simply on a GaAs substrate. In order to realize characteristic impedance of under 20 Ω, conventional CPW's must have narrow slot width of less than 5 μm and wide center conductor width of over 300 μm. Therefore, in terms of chip size reduction and to avoid the difficulties in narrow slots processing, conventional CPW's are not suitable for realizing low characteristic impedance.

To provide CPW's with low characteristic impedance, Gillick and Robertson demonstrated a new CPW structure with multilayered conductors, and exhibited characteristic impedance of as low as 9 Ω [2]. In this paper, we propose another structure more similar to conventional CPW's that can realize low characteristic impedance. The idea here is that the total dielectric constant under the conductors is made higher than that of the conventional CPW by using a high dielectric-constant material. If the CPW has a thin film with high dielectric constant underneath the conductors, the capacitance per unit length of CPW would become higher, which leads lower characteristic impedance than that of conventional CPW. We chose $SrTiO_3$ (STO) as a high dielectric material because STO has already been used as an insulator for bypass capacitors to reduce the MMICs' capacitor area [3] and it is more applicable for MMIC technology than any other high dielectric materials.

In the following, we show the experimental results of the CPW's fabricated with a STO thin film on GaAs (STO CPW's) and then discuss about the performance of STO CPW's.

II. Fabrication and Measurement

The STO CPW was fabricated as follows. First, an STO thin film was deposited on a GaAs substrate by RF magnetron sputtering. The deposition conditions were substrate temperature of 300 °C and RF power of 500 W, with a deposition rate of 0.35 μm/h. The center conductors and ground planes that consisted of 2 μm-thick Ti/Au were then formed on the STO thin film by using evaporation and electroplating methods. Fig. 1 shows the cross section of the investigated CPW's. The widths of center conductors and ground planes were 50 and 500 μm, respectively, and the length was 2 mm. The STO film thickness was 1 μm. The S-parameters were measured with a vector network analyzer up to 60 GHz.

Characteristic impedances were determined by using a circuit simulator of the Hewlett-Packard Microwave Design System (HP-MDS). Small-signal sources were connected to the measured S-parameters on HP-MDS and real parts of the source impedance were optimized to make the return loss show the lowest. Fig. 2 shows the dependence of the measured characteristic impedance on the slot width in the STO CPW and the conventional CPW. The STO CPW's exhibits characteristic impedance about 10 Ω lower than that of the conventional one throughout the entire slot width and is reduced with decreasing slot width down to 18 Ω. Using the $\lambda/4$ transmission line with this characteristic impedance, the load impedance of 6 Ω is transformed into an input impedance of around 50 Ω according to the well-known formula $Z_{\rm in}Z_L = Z_o^2$, where $Z_{\rm in}$ denotes input impedance, Z_L load impedance, and Z_o characteristic impedance of transmission lines. The value of 6 Ω corresponds approximately to the real part of the input impedance of 600-μm gatewidth FET's.

III. Discussion

With a circuit simulator, it is possible to extract the total relative dielectric constants of the substrate, including both the STO thin film and the GaAs substrate, from the measured S-parameters. We conducted the fitting between the measured and simulated data with varying the relative dielectric constant of the substrate. The STO CPW with 5-μm-width slots was found to exhibit a total relative dielectric constant as high as 33. This value is about three times higher than that of the conventional CPW. With this value, we estimated the available lowest characteristic impedance of STO CPW's with the slot-width constant at 5 μm by varying center conductor width. The impedance would decrease down to 12.6 Ω with an increase of center conductor width up to 300 μm, as shown in Fig. 3. This means that a load impedance of 3 Ω would be transformed into about 50 Ω with the $\lambda/4$ impedance transformer. Fig. 4 shows the extracted relative dielectric constants for another slot widths. The figure shows that the narrower slot CPW's tend to have higher dielectric constants. This is because when the slots become narrower, the electric field concentrates more to the surface, and the high dielectric constant of an STO thin film contributes more to the total relative dielectric constant. This fact helps the STO CPW's to have the low-impedance characteristics in narrow slots.

We next evaluated the relative dielectric constant of the fabricated STO thin film by using a conventional electromagnetic simulator of

Manuscript received July 14, 1999.

The authors are with the Electronics Research Laboratory, Matsushita Electronics Corporation, Osaka 570-8501, Japan (e-mail: tanabe @oerl.src.mei.co.jp).

Publisher Item Identifier S 0018-9480(00)03759-5.

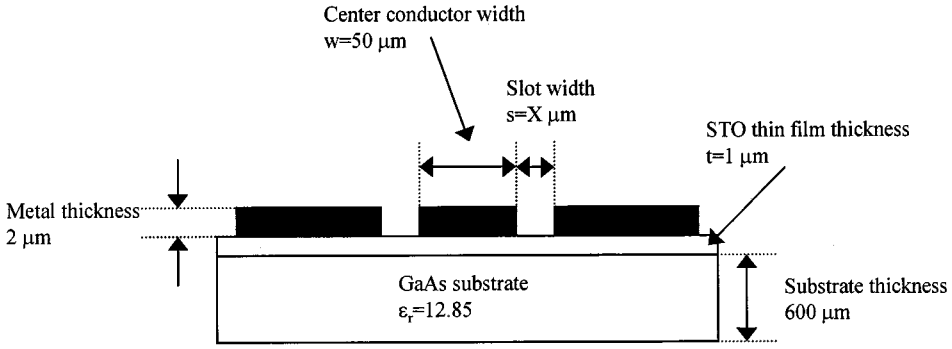

Fig. 1. Schematic figure of the implemented STO CPW.

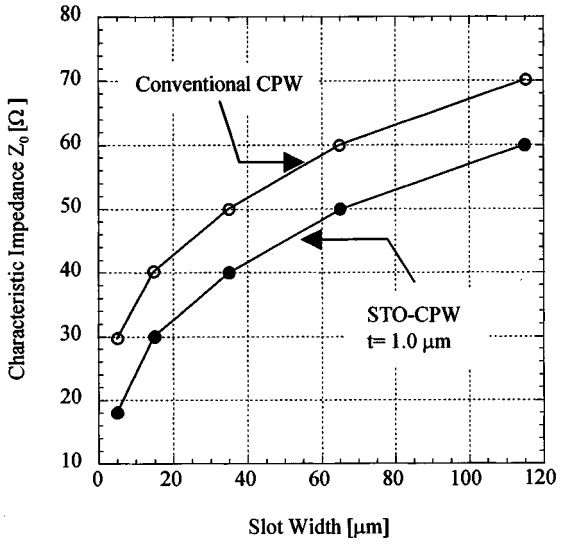

Fig. 2. Characteristic impedance of the fabricated STO CPW's and the conventional CPW's with center conductor width of 50 μm.

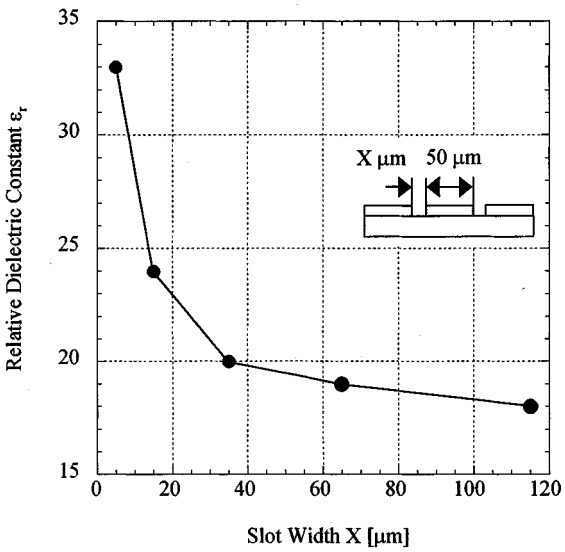

Fig. 4. Available characteristic impedance of the STO CPW's for its center conductor widths.

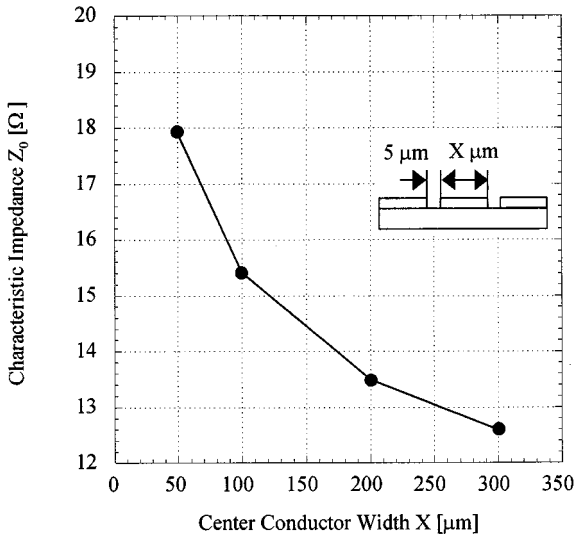

Fig. 3. Relative dielectric constant derived from the fabricated STO CPW's.

the Hewlett-Packard High Frequency Simulation System (HP-HFSS). The simulated structure was the same as shown in Fig. 1. The assumed relative dielectric constants of STO thin film were 100, 200, and 300. The relative dielectric constant of 300 correspond to that of an STO bulk substrate, whose value was extracted from the CPW fabricated on an STO bulk substrate by using a circuit simulator as mentioned in the previous section. The dependence of the characteristic impedance on the slot width of both the simulation and experiment is shown in Fig. 5. The experimental data falls between the two sets of the simulated data with the dielectric constant of 100 and 200. From this, we may conclude that the relative dielectric constant of the fabricated STO thin film was between 100–200. This value is far below that of the bulk STO. Since the crystalline structure and lattice constant of the STO differs from that of GaAs, an STO thin film on GaAs is assumed to have poorer crystallinity and lower relative dielectric constant than a bulk STO substrate. By improving the crystallinity of the STO thin film, still higher dielectric constant and lower characteristic impedance may be achieved. If a relative dielectric constant of near 300 were to be achieved, the characteristic impedance of an STO CPW with the slot width of 5 μm and the center conductor width of 300 μm could be reached as low as 10.5 Ω.

For transmission lines, losses are also important characteristic. We investigated losses of 30-Ω lines on both the STO CPW and the conventional CPW. The STO CPW with 30-Ω characteristic impedance consisted of 50-μm-width center conductor and 15-μm-width slots, while the conventional one with the same impedance consisted of

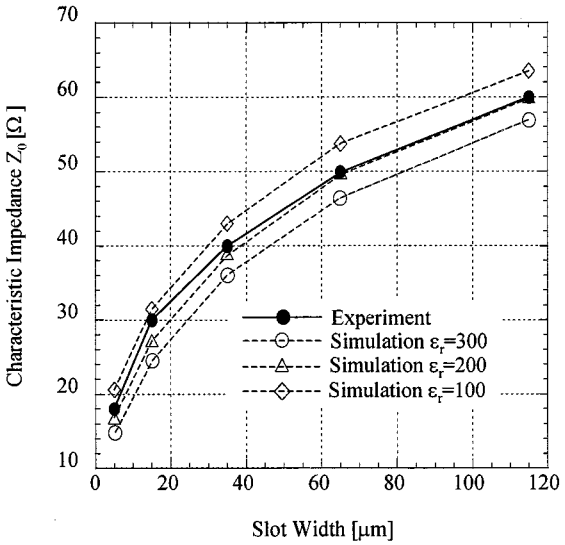

Fig. 5. Characteristic impedance of the measured STO CPW's and the simulated STO CPW's with ε_r of 100, 200, and 300.

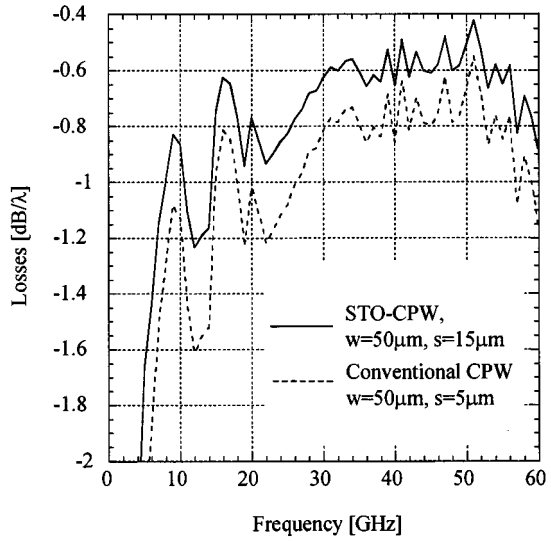

Fig. 6. Losses of the STO CPW and the conventional CPW in characteristic impedance of 30 Ω.

50-μm-width center conductor and 5-μm-width slots. Fig. 6 shows losses per unit guide wavelength of the STO CPW and the conventional CPW. As can be seen from Fig. 6, the losses of the STO CPW is lower than the conventional CPW throughout the measured frequency range.

Additionally, from the following relation on the guide wavelength, the distributed elements for MMIC's could be shorten if STO CPW's were utilized, due to its high dielectric constant:

$$\frac{\lambda_{\text{STO-CPO}}}{\lambda_{\text{conventional-CPW}}} = \frac{\sqrt{\varepsilon_{\text{conventional-CPW}}}}{\sqrt{\varepsilon_{\text{STO-CPW}}}}.$$

For example, in comparison with 30-Ω lines for both the CPW's at 30 GHz, the STO CPW has a dielectric constant of 24 and the $\lambda/4$ of 0.7 mm, while the conventional one has a dielectric constant of 12.85 and the $\lambda/4$ of 1 mm. The STO CPW could shorten the distributed elements by at least 30%.

IV. Conclusion

We have demonstrated the characteristics of the CPW fabricated with an STO thin film (STO CPW) on GaAs for the first time. It exhibited the impedance of as low as 18 Ω with a center conductor width of 50 μm and the slot width of 5 μm, while the conventional CPW showed 30 Ω with the same configuration. With the wider center conductor of 300-μm width, the impedance decreases to 12.6 Ω. By using a $\lambda/4$ impedance transformer, the load impedance of 3 Ω could be transformed into about 50 Ω. The STO CPW's exhibit lower loss characteristic than that of the conventional one. Therefore, the STO CPW's would be applicable and useful enough for the matching networks for power MMIC's or the other low-impedance devices.

Acknowledgment

The authors wish to express their sincere thanks to Dr. M. Kazumura, Matsushita Electronics Corporation, Osaka, Japan, and Dr. D. Ueda, Matsushita Electronics Corporation, Osaka, Japan, for their continuous encouragement throughout this work. Special thanks go to Dr. G. Tohmon, Matsushita Electronics Corporation, Osaka, Japan, for his valuable suggestion in the preparation of this paper's manuscript.

References

[1] T. Sporkmann, "The evolution of coplanar MMIC's over the past 30 years," *Microwave J.*, pp. 96–111, July 1998.

[2] M. Gillick and I. D. Robertson, "Ultra low impedance CPW transmission lines for mutilayer MMIC's," in *IEEE MTT-S Int. Microwave Symp. Dig.*, 1993, pp. 145–148.

[3] M. Nishitsuji, A. Tamura, K. Yahata, M. Shibuya, M. Kitagawa, and T. Hirao, "New GaAs–MMIC process technology using low-temperature deposited $SrTiO_3$ thin film capacitors," *Electron. Lett.*, vol. 30, no. 13, pp. 1045–1046, June 1994.

Gradient Evaluation for Neural-Networks-Based Electromagnetic Optimization Procedures

G. Antonini and A. Orlandi

***Abstract*—This paper extends the use of a neural network (NN) approximating a function, to the evaluation of the gradient of the same function. This is done without any extra training of the network. The evaluation of the function's gradient is used in NN-based optimization procedures in order to speed up the convergence and to maintain the overall accuracy.**

***Index Terms*—Modeling, neural network, optimization methods.**

I. Introduction

Artificial neural networks (NN's) are playing an ever increasing role in the optimization techniques of a wide set of electromagnetic structures. Among the major papers dealing with this issue, [1]–[4] and

Manuscript received July 22, 1999.

The authors are with the Department of Electrical Engineering, University of L'Aquila, I-67040, Poggio di Roio, L'Aquila, Italy (e-mail: antonini@ing.univaq.it; orlandi@ing.univaq.it).

Publisher Item Identifier S 0018-9480(00)03760-1.

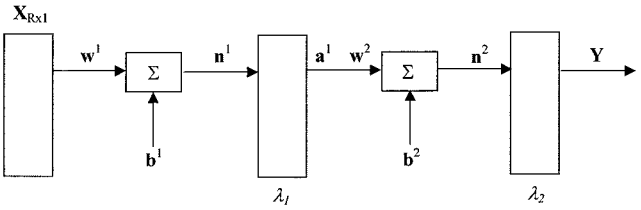

Fig. 1. Three-layer FF NN.

their respective references can be considered. An optimization procedure is substantially the maximization (minimization) of a function $\mathbf{Y} = f(\mathbf{X})$, in which $\mathbf{X}$ is the input vector containing the design parameters that can be changed in order to obtain the output vector $\mathbf{Y}$ containing the parameters for which the maximum (minimum) should be obtained. $f(\cdot)$ is the model that relates $\mathbf{Y}$ to $\mathbf{X}$. In an NN approach, the function $f(\cdot)$ is mapped by an NN with an enormous saving of computing time and memory requirements with respect to other traditional modeling and simulation techniques to be optimized.

A large class of numerical multidimensional optimization methods can be described by the following logic steps: start at a point $\mathbf{X}_0$, as many times as needed move from point $\mathbf{X}_i$ to point $\mathbf{X}_{i+1}$ by minimizing $f(\mathbf{X})$ along the line from $\mathbf{X}_i$ in the direction of the local downhill gradient $-\nabla f(\mathbf{X}_i)$. Hence, it is necessary to evaluate the function's gradient at arbitrary points. When $f(\cdot)$ is not analytically known, as in the case of the NN mapping, the gradient is evaluated by recurring to finite-differences schemes whose accuracy is often not sufficient (due to roundoff or truncation errors) to point the way to the maximum (minimum).

This paper proposes a way to evaluate the function's gradient only by means of the trained NN designed and used for the function's approximation during the optimization. This procedure maintains the same level of accuracy in the approximation without any significant increasing of the computing requirements.

II. NN Gradient Evaluation

Let's consider an already trained three-layer feedforward (FF) NN such as that in Fig. 1. It has R inputs $\mathbf{X} = [x_1 \ \cdots \ x_R]^t$ and two layers: the hidden layer has S neurons and the output layer has T neurons. The outputs $\mathbf{Y} = [y_1 \ \cdots \ y_T]^t$ are also T. Assigning the identification number 1 to the hidden layer and number 2 to the output one, the activation functions are

$$\mathbf{a}^1 = \lambda_1(\mathbf{n}^1) \tag{1a}$$

$$\mathbf{Y}^2 = \lambda_2(\mathbf{n}^2) \tag{1b}$$

in which $\mathbf{n}^1$ and $\mathbf{n}^2$ are their local inputs

$$\mathbf{n}^1_{S\times 1} = \mathbf{W}^1_{S\times R}\mathbf{X}_{R\times 1} + b^1_{S\times 1} \tag{2a}$$

$$\mathbf{n}^2_{T\times 1} = \mathbf{W}^2_{T\times S}\mathbf{a}^1_{S\times 1} + b^2_{T\times 1} \tag{2b}$$

where $\mathbf{W}^i$ and $\mathbf{b}^i$ are the matrices containing the weights and biases of the network of the ith layer and subscripts signify the dimensions of these matrices. The gradient of $f(\cdot)$, mapped by the NN and evaluated at the arbitrary point $\mathbf{X}_k$, is written as

$$\begin{aligned}\nabla f(\mathbf{X}_k) &= \frac{\partial \mathbf{Y}}{\partial \mathbf{X}_{T\times R}} \\ &= \frac{\partial \mathbf{Y}}{\partial \mathbf{n}^2_{T\times T}}\frac{\partial \mathbf{n}^2}{\partial \mathbf{X}_{T\times R}} \\ &= \frac{\partial \mathbf{Y}}{\partial \mathbf{n}^2_{T\times T}}\frac{\partial \mathbf{n}^2}{\partial \mathbf{a}^1_{T\times S}}\frac{\partial \mathbf{a}^1}{\partial \mathbf{X}_{S\times R}} \\ &= \frac{\partial \mathbf{Y}}{\partial \mathbf{n}^2_{T\times T}}\frac{\partial \mathbf{n}^2}{\partial \mathbf{a}^1_{T\times S}}\frac{\partial \mathbf{a}^1}{\partial \mathbf{n}^1_{S\times S}}\frac{\partial \mathbf{n}^1}{\partial \mathbf{X}_{S\times R}}.\end{aligned} \tag{3}$$

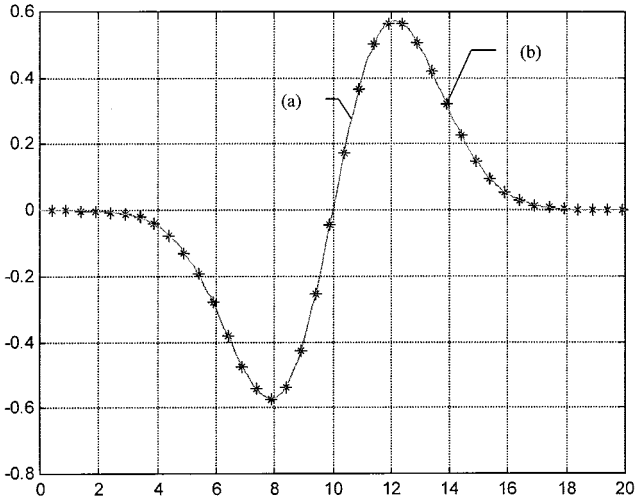

Fig. 2. Derivative of (6). (a) Analytical. (b) Evaluated by means of (3).

From (2), one obtains

$$\frac{\partial \mathbf{n}^1}{\partial \mathbf{X}} = \mathbf{W}^1 \tag{4a}$$

$$\frac{\partial \mathbf{n}^2}{\partial \mathbf{a}^1} = \mathbf{W}^2 \tag{4b}$$

and

$$\frac{\partial \mathbf{a}^1}{\partial \mathbf{n}^1} = \frac{\partial \lambda_1}{\partial \mathbf{n}^1} = \operatorname{diag}\left[\frac{\partial \lambda_1}{\partial n^1_1} \quad \cdots \quad \frac{\partial \lambda_1}{\partial n^1_S}\right] \tag{5a}$$

$$\frac{\partial \mathbf{Y}}{\partial \mathbf{n}^2} = \frac{\partial \lambda_2}{\partial \mathbf{n}^2} = \operatorname{diag}\left[\frac{\partial \lambda_2}{\partial n^2_1} \quad \cdots \quad \frac{\partial \lambda_2}{\partial n^2_T}\right]. \tag{5b}$$

The derivatives in (5) are analytically calculated in closed form because the activation functions are known. These derivatives depend on $\mathbf{n}^1$ and $\mathbf{n}^2$, which are evaluated by means of (2). By substituting (4) and (5) in (3), one obtains an algebraic expression to evaluate $\nabla f(\mathbf{X}_k)$.

As a test, Fig. 2 shows the comparison between the derivative with respect to x of the simple function

$$f(x) = e^{-\left(\frac{x-\sigma}{3}\right)^2} \tag{6}$$

evaluated analytically and the derivative evaluated by means of (3) from an FF NN, with six neurons in the hidden layer, trained to approximate (6). The two curves overlap one another and the percentage difference between them is less than 0.01%.

Expression (3) for the function's gradient can be generalized for an FF NN with multiple layers in the following form:

$$\nabla f(\mathbf{X}_k) = \prod_{i=1}^{N_a}\frac{\partial \lambda_i}{\partial \mathbf{n}^i}\mathbf{W}^i \tag{7}$$

in which N_a is the number of activation functions.

III. Numerical Application

As an example, consider the printed circuit board (PCB) shown in Fig. 3, consisting of four copper ($\sigma_{\mathrm{cu}} = 5.8\cdot 10^7$ S/m) traces of equal width $w = 360$ μm, thickness $t = 36$ μm and height $h = 1.2$ mm on the reference infinite perfectly conductive ground plane. The dielectric constant is $\varepsilon_r = 4.7$ (glass epoxy). Each one of the lands is length $l = 12$ cm and terminated at both ends on a resistive load $R_L = 117\ \Omega$. The voltage source is at one end of conductor 1: it has a trapezoidal shape with amplitude $V_S = 1$ V, $\tau_r = \tau_f = 50$ ps, period $T = 400$ ps, and duty cycle $\delta = 0.5$. Conductors 1 and 3 are

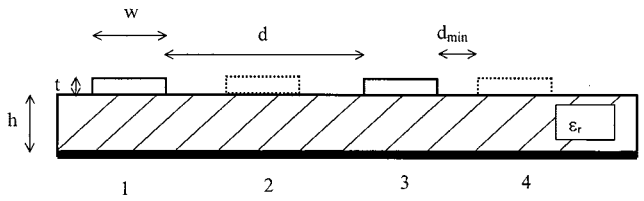

Fig. 3. Four-conductor PCB.

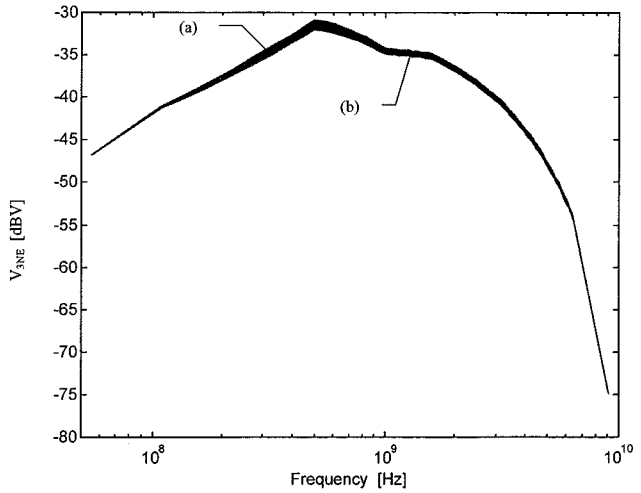

Fig. 4. Near-end crosstalk on conductor 3. (a) Upper bound. (b) Lower bound.

fixed at an edge-to-edge separation distance $d = 2.52$ mm, conductors 2 and 4 can be moved and their minimum distance to 1 and/or 3 is $d_{\min} = 127$ μm. The goal is to find the position of 2 and 4 in order to minimize the near-end crosstalk $V_{3\mathrm{NE}}$ on conductor 3. The per unit length (p.u.l.) parameters of this multiconductor transmission line are evaluated by means of the software in [5] for 50 possible positions of 2 and 4. An FF NN has then been trained to evaluate $V_{3\mathrm{NE}}$. This NN is used in a variable metric method [6] minimization procedure requiring the evaluation of gradients. As described in [2] and [3], the usage of an NN as a function model speeds up the optimization; in this example, a saving of computing time around the 70% has been noticed with respect to the usage, for the same problem, of a traditional simulator to evaluate $V_{3\mathrm{NE}}$. In the proposed example, in 15% of the cases, a better convergence to the minimum is obtained than when the function's gradient is approximated by finite differences. Among the useful results of the analysis of the configuration in Fig. 3, Fig. 4 shows the variation band with the upper and lower limits of the crosstalk $V_{3\mathrm{NE}}$ for all possible positions of conductors 2 and 4 with respect to 1 and 3.

IV. Conclusion

The evaluation of the function's gradient by means of the same weights and biases of an FF NN approximating the function has been shown to be a useful tool in order to decrease the computing efforts during NN-based optimization procedures of electromagnetic structures. Furthermore, the computational accuracy is preserved because, in this way, there is no need to make recourse to a finite-difference approximation of the derivatives.

References

[1] A. H. Zaabab, Q. Zhang, and M. Nakhla, "A neural network modeling approach to circuit optimization and statistical design," *IEEE Trans. Microwave Theory Tech.*, vol. 43, pp. 1349–1358, June 1995.

[2] A. Veluswami, M. Nakhla, and Q. Zhang, "The application of neural network to EM-based simulation and optimization of interconnects in high-speed VLSI circuits," *IEEE Trans. Microwave Theory Tech.*, vol. 45, pp. 712–722, May 1997.

[3] J. W. Bandler *et al.*, "Electromagnetic optimization of 3-D structures," *IEEE Trans. Microwave Theory Tech.*, vol. 45, pp. 770–779, May 1997.

[4] M. Vai, S. Wu, B. Li, and S. Prasad, "Reverse modeling of microwave circuits with bidirectional neural network models," *IEEE Trans. Microwave Theory Tech.*, vol. 46, pp. 1492–1494, Oct. 1998.

[5] C. R. Paul, *Analysis of Multiconductor Transmission Lines*. New York: Wiley, 1994.

[6] W. H. Press, B. P. Flannery, S. A. Teukolsky, and W. T. Vetterling, *Numerical Recipes: The Art of Scientific Computing*. Cambridge, U.K.: Cambridge Univ. Press, 1989.

Analysis of Hollow Conducting Waveguides Using Superquadric Functions—A Unified Representation

Sheng-Li Lin, Le-Wei Li, Tat-Soon Yeo, and Mook-Seng Leong

***Abstract*—Waveguides of various geometries have found many applications. The analysis of the wave modes inside these waveguides are usually subject to cross sections of the waveguides and specific, but convenient, coordinates systems have to be chosen in the analysis. In this paper, the boundary geometries of waveguides (which include rectangular, circular, elliptical, triangular, coaxial, etc.) are represented in a unified manner by a superquadric function. In this paper, with the Rayleigh–Ritz method, the wave propagation characteristics in a hollow conducting waveguide of the superquadric cross section are analyzed in a unified manner. From the analysis, it is realized that the superquadric function can be utilized to accurately model the boundary of various waveguide structures through variation of the shape parameters. The comparisons between the analytical and computational results show this method is accurate and efficient.**

***Index Terms*—Guided waves, Rayleigh–Ritz method, waveguide analysis, waveguide modes.**

I. Introduction

The electromagnetic wave propagation characteristics in conducting waveguides has been intensively studied in the past several decades [1], [2]. When the waveguide geometric shapes are simple and regular, the conventional mode-matching method can be used. The integral-equation method, the finite-element method, or other numerical techniques must be used when the cross-sectional shape becomes complicated or the dielectric loading is inhomogeneous. The integral equation method needs small computational storage, but it becomes quite complicated to solve multimaterial problems. The finite-element method can handle

Manuscript received April 20, 1999. This work was supported by the Ministry of Defence–National University of Singapore Research and Development Commission under Research Grant GR6521.

The authors are with the Communications and Microwave Division, Department of Electrical Engineering, National University of Singapore, Singapore 119260 (e-mail: LWLi@nus.edu.sg).

Publisher Item Identifier S 0018-9480(00)03762-5.

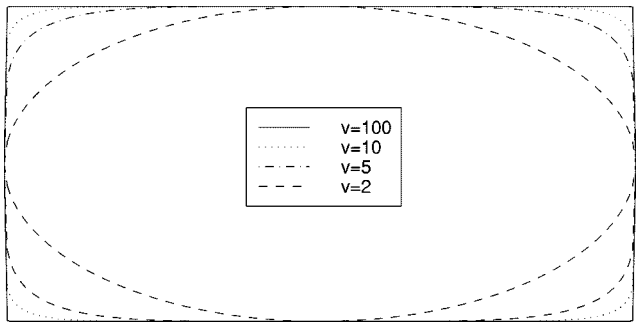

Fig. 1. Superquadric representation of waveguide cross-sectional geometry for $\gamma = 2, 5, 10$ and 100 and at $a/b = 2$.

waveguide problems with irregular cross-sectional shapes and the problems with multimaterials, but it generates spurious modes that need to be overcome.

In the literature [3], the Rayleigh–Ritz method with the entire polynomial basis functions was presented to analyze hollow elliptical waveguide modes. The Rayleigh–Ritz method was proven to be a straightforward, robust, and accurate technique, and the complete polynomial trial functions were used to ensure the field equations in the inscribed polygon of the ellipse to be satisfied. Furthermore, the orthogonal polynomial method has been used successfully in the analysis of TM modes of polygonal cross-sectional waveguides [4]. Further, in [5], the polynomial method without the requirement of orthogonality has been proposed to analyze the elliptical waveguide, and the polynomials are directly used to describe the ellipse instead of its inscribed polygon.

In this paper, the superquadric representation, which can accurately model a wide variety of different shapes in one unified formulation [6], is used to describe the cross section of the waveguide. The superquadric representation can be seen as the extension of the constraint function in [4] and [5]. The wave propagation characteristics in rectangular, circular, and elliptical cross-sectional waveguides are analyzed by the Rayleigh–Ritz method in the unified manner. In addition, some other cross-sectional waveguides are also studied in this paper by this method. For instance, the triangular and coaxial cross-section waveguides are also analyzed in a similar manner by combining the superquadric function and polynomials to describe the waveguide geometries. In short, a wide range of waveguides can be analyzed in this unified method. Both TE and TM modes in the conducting waveguides have been studied. The cutoff wavenumbers obtained here are compared with those exact results and a very good agreement is found.

II. General Mathematical Algorithm

A. Superquadric Representation of Waveguide Cross Sections

A superquadric function has the following form:

$$\left|\frac{x}{a}\right|^{\gamma} + \left|\frac{y}{b}\right|^{\gamma} - 1 = 0 \tag{1}$$

where a and b are the semiaxes in the x and y directions, respectively, and γ is a "squareness parameter," which controls the behavior of the loop radius of curvature. Fig. 1 illustrates the effects of the squareness parameter on the geometry of the waveguide for $\gamma = 2, 5, 10$, and 100 and an aspect ratio of $a/b = 2$. As can be seen from the variations, a value of $\gamma = 2$ corresponds to an ellipse, while the loop squareness increases with γ. When $\gamma = 10$, the corresponding geometry is a rectangular one with rounded corners. When $\gamma = 100$, the corresponding geometry becomes rectangular. It is evident that the superquadric representation can be utilized to model numerous waveguides of different cross-sectional configurations through variation of the shape parameters a, b, and γ. Also, the function itself is capable of providing rounded corners on a rectangular shape and allows accurate representation of many other practical geometries.

B. Rayleigh–Ritz Procedure and Polynomial Functions

For the cylindrical waveguide of uniform cross section, the z-dependent electromagnetic fields can be expressed by $e^{jk_z z}$. The cutoff wavenumber k_c can be obtained by letting $k_z = 0$. The wave equation for the longitudinal component of the electric and magnetic fields is

$$\nabla_T^2 \begin{bmatrix} E_z \\ H_z \end{bmatrix} + k_c^2 \begin{bmatrix} E_z \\ H_z \end{bmatrix} = 0 \tag{2}$$

where ∇_T^2 represents the Laplacian operation in transverse plane. The Dirichlet and Neumann boundary conditions for TM and TE waves are written as

$$E_z|_D = 0 \tag{3}$$

$$\left.\frac{\partial H_z}{\partial n}\right|_D = 0 \tag{4}$$

where D denotes the boundary of the waveguide and $\hat{\boldsymbol{n}}$ stands for the normal direction of the cross section.

The Rayleigh–Ritz procedure is employed by setting the energy w as a function of u (representing either E_z or H_z) as follows:

$$w(u) = \frac{1}{2}\int\int_D \left[\left(\frac{\partial u}{\partial x}\right)^2 + \left(\frac{\partial u}{\partial y}\right)^2\right] dx\,dy - \frac{k_c^2}{2}\int\int_D u^2\,dx\,dy. \tag{5}$$

Express the field u as a series of polynomials

$$u(x, y) = \sum_{i=1}^{m} C_i \phi_i. \tag{6}$$

Substituting (6) into (5) and minimizing the energy function w due to c_i, we obtain

$$[\boldsymbol{K}][\boldsymbol{C}]^T = k_c^2[\boldsymbol{M}][\boldsymbol{C}] \tag{7}$$

where the matrix elements are given by

$$k_{i,j} = \iint_D \left(\frac{\partial \phi_i}{\partial x}\frac{\partial \phi_j}{\partial x} + \frac{\partial \phi_i}{\partial y}\frac{\partial \phi_j}{\partial y}\right) dx\,dy \tag{8}$$

and

$$m_{i,j} = \iint_D \phi_i \phi_j\,dx\,dy. \tag{9}$$

It should be pointed out herein that numerical solutions to the two integrations in (8) and (9) can be obtained for any given γ quantity in general while the analytical solutions to them can be derived for some special cases.

For the TM case, we have

$$\phi_i(x, y) = \psi(x, y) f_i(x, y) \tag{10}$$

and for the TE case

$$\phi_i(x, y) = f_i(x, y). \tag{11}$$

The $\psi(x, y)$ is the constraint function for the waveguide cross sections, which satisfies the boundary conditions given by (3), while the Neumann boundary condition in (4) can be automatically satisfied by the polynomial functions themselves in (11).

We construct the function $f_i(x, y)$ in the following way.

TABLE I
CUTOFF WAVENUMBERS (k_c) OF TM WAVES IN A CIRCULAR WAVEGUIDE FOR (DEG = 9)

TM mode	Exact	Calculated	Error (%)
(0,1)	2.4048	2.4046	0.008
(1.1)	3.8317	3.8320	0.01
(2,1)	5.1356	5.1376	0.04
(0,2)	5.5250	5.5265	0.12
(3,1)	6.3802	6.3792	0.016
(1,2)	7.0156	7.0032	0.18
(4,1)	7.5883	7.6038	0.20
(2,2)	8.4172	8.4226	0.07
(0,3)	8.6531	8.6272	0.30
(5,1)	8.7715	8.7675	0.50

- Let

$$r = \mathrm{Int}\left(\sqrt{i-1}\right) \tag{12}$$

where the $\mathrm{Int}(\cdot)$ function takes the integer part of the argument.

- Define

$$t = (i-1) - r^2. \tag{13}$$

- Thus, when t is even

$$s = \frac{t}{2} \quad \text{and} \quad f_i(x, y) = x^r y^s \tag{14}$$

and when t is odd

$$s = \frac{t-1}{2} \quad \text{and} \quad f_i(x, y) = x^s y^r. \tag{15}$$

The function $f_i(x, y)$ has a degree of $r + s$.

III. COMPUTATIONAL RESULTS

A. Cutoff Wavenumbers in Rectangular, Circular, and Elliptical Waveguides

For rectangular, circular, and elliptical cross-sectional waveguides, the constraint function in (10) can be directly represented by the superquadric function

$$\psi = \left|\frac{x}{a}\right|^\gamma + \left|\frac{y}{b}\right|^\gamma - 1. \tag{16}$$

The relationships between the shape parameters and geometries are given, for instance, by the following. For $\gamma = 2$

$$\begin{cases} a = b, & \text{circular} \\ a \neq b, & \text{elliptical} \end{cases} \tag{17}$$

and for $\gamma = 100$

$$\begin{cases} a = b, & \text{square} \\ a \neq b, & \text{rectangular.} \end{cases} \tag{18}$$

The cutoff wavenumbers of TM waves in a circular waveguide, the cutoff wavelength of the TE_{11} mode in an elliptical waveguide and the cutoff wavenumbers of TE waves in a rectangular waveguide are calculated and compared with the exact analytical results, as shown in Tables I–III. The constraint function in [5] is the same as in (17) and can be considered as a special case of superquadric representations.

As for the convergence and accuracy, detailed discussions for the analysis have been provided in [5] for an elliptical waveguide. Even so, we have carefully checked them again in the present studies. It is realized that the convergence is quite fast and only a polynomial of degree 9 is required to achieve the accuracy of a maximum relative error of 0.9%.

TABLE II
CUTOFF WAVELEGNTH OF EVEN TE_{11} WAVES IN AN ELLIPTICAL WAVEGUIDE FOR (DEG = 8)

Eccentricity	Exact	Calculated	Error (%)
0.21704127	3.4093	3.4081	0.03
0.59049548	3.3870	3.3858	0.031
0.95078586	3.3395	3.3384	0.032

TABLE III
CUTOFF WAVENUMBERS OF TE WAVES IN A RECTANGULAR WAVEGUIDE FOR ($a = b$ AND DEG = 9)

TE mode	Exact	Calculated	Error (%)
(0,1)(1,0)	1.5708	1.5708	1.30e-5
(1,1)	2.2214	2.2214	1.32 e-5
(2,0)(0,2)	3.1416	3.1416	1.67e-3
(1,2)(2,1)	3.5124	3.5124	1.35e-3
(2,2)	4.4429	4.4429	1.67e-3
(3,0)(0,3)	4.7124	4.7134	0.02
(1,3)(3,1)	4.9673	4.9695	0.04
(2,3)(3,2)	5.66358	5.6712	0.13
(4,0)(0,4)	6.2832	6.2833	1.67e-3
(1,4)(4,1)	6.4766	6.4791	0.004

TABLE IV
CUTOFF WAVENUMBERS (k_c) OF DOMINANT TE AND TM MODES IN OTHER SUPERQUADRIC WAVEGUIDES FOR (DEG = 5)

γ	3	4	6	7	8	50
TE	1.726	1.672	1.624	1.612	1.603	1.571
TM	2.284	2.249	2.231	2.227	2.224	2.223

Using the superquadric representation as the constraint function, we can also calculate the cutoff wavenumbers in waveguides of other shaped cross sections whose analytical results are difficult to obtain. This can be achieved simply by varying the superquadric function shape parameter γ. The cutoff wavenumbers of the dominant TE and TM modes for some other geometries are shown in Table IV.

B. Cutoff Wavenumbers in Coaxial and Triangular Waveguides

Instead of using superquadric representation directly, we can also combine superquadric function and simple polynomials to describe the waveguide geometries. In this section, the triangular and coaxial waveguides are analyzed in the similar manner as an example.

For coaxial waveguide, the constraint function takes the following form:

$$\psi = \left(\left|\frac{x}{a_1}\right|^\gamma + \left|\frac{y}{b_1}\right|^\gamma - 1\right)\left(\left|\frac{x}{a_2}\right|^\gamma + \left|\frac{y}{b_2}\right|^\gamma - 1\right) \tag{19}$$

where, when $\gamma = 2$, $a_1 = b_1 = a$ denotes the radius of the inner circle, and $a_2 = b_2 = b$ represents the radius of the outer circle of a coaxial waveguide. From (19), we can see that ψ can satisfy the boundary condition given by (3) at both the inner and outer circular boundaries. The coaxial waveguide can be analyzed in the very similar procedure given previously. The cutoff wavelengths of the dominant TE mode (i.e., TE_{11} mode) in the coaxial waveguides for different ratios of c (defined as b/a) are calculated and shown in Table V. In Table VI, the first ten cutoff wavelengths of TM modes in a coaxial waveguide for a ratio of $c = b/a = 2$ are shown and compared with the exact and analytical results. The two sets of results obtained agree well, as can be seen from the comparison.

For a triangular waveguide, the procedure used is the same as before and the only difference in the calculation is the change of the constraint

TABLE V
CUTOFF WAVELEGNTHS OF TE_{11} WAVES IN A COAXIL WAVEGUIDE (DEG = 8)

c	Exact	Calculated	Error (%)
1.4	7.5060	7.4313	0.9
1.5	7.8033	7.8434	0.5
1.6	8.0953	7.9441	1.9
2.0	9.2809	9.1633	1.3
2.5	10.7379	10.7645	0.3
3.0	12.2241	12.1831	0.3
3.5	13.7454	13.5524	1.4
4.0	15.2876	15.2646	0.15

TABLE VI
CUTOFF WAVELEGNTHS OF TM IN A COAXIL WAVEGUIDE FOR ($c = b/a = 2$, and DEG = 7)

TM mode	Exact	Calculated	Error (%)
(0,1)	2.0119	2.0118	0.005
(1,1)	1.9653	1.9643	0.05
(2,1)	1.8480	1.8358	0.7
(3,1)	1.6982	1.6633	2.1
(0,2)	1.0016	0.9972	0.4
(1,2)	0.9954	0.9905	0.5
(2,2)	0.9772	0.9571	2.1
(3,2)	0.9491	0.9118	4.0
(0,3)	0.6671	0.6744	1.0
(1,3)	0.6653	0.6493	2.5

TABLE VII
CUTOFF WAVENUMBERS OF TM MODES IN A RIGHT-TRIANGULAR WAVEGUIDE OF THE DIMENSIONS ($a \times \sqrt{2.5}\,a \times \sqrt{2.5}\,a$) for (DEG = 7)

TM mode	Calculated (k_c)	Results in [4]	Error (%)
	1.5446		
	5.4493		
(1,1)	5.7097	5.72	0.18
	6.7904		
(1,2)	8.2896	8.20	1.09
	8.4184		
(2,1)	9.1584	9.36	2.1
	12.2649		

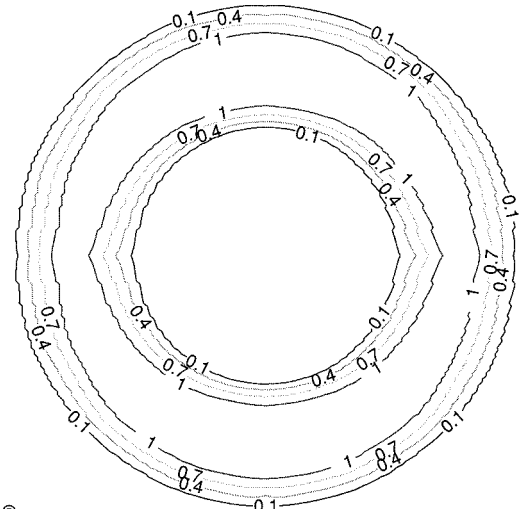

Fig. 2. E_z-field contour of the TM_{01} mode in a coaxial waveguide for ($b/a = 2$).

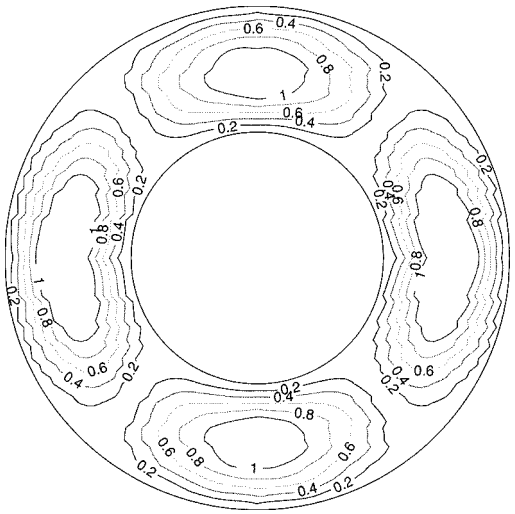

Fig. 3. E_z-field contour of the TM_{21} mode in a coaxial waveguide for ($b/a = 2$).

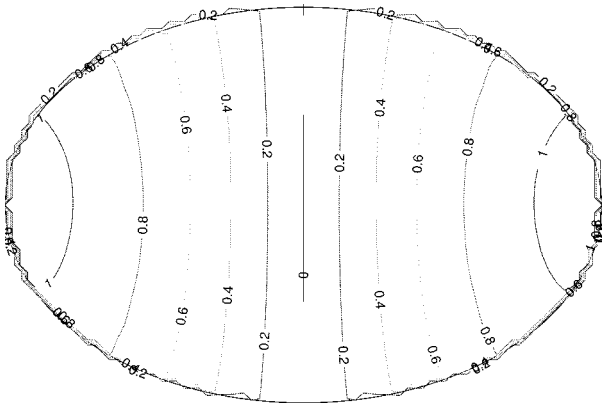

Fig. 4. H_z-field contour of the TE_{11} mode in an elliptical waveguide with eccentricity of 0.75.

function. The constraint function can be now constructed by the superquadric representation and a straight line, given as follows:

$$\psi = x\left(\left|\frac{x}{a}\right|^{\gamma} + \left|\frac{y}{b}\right|^{\gamma} - 1\right) \tag{20}$$

where $\gamma = 1$. The cutoff wavenumbers of the right-triangular ($a \times \sqrt{2.5}\,a \times \sqrt{2.5}\,a$) waveguide of a TM mode are calculated and shown in Table VII.

Using (6) and (7), we have obtained the field distribution patterns of both TM and TE modes in various kinds of waveguides. Two field contours of TM modes in a coaxial waveguide and one field contour of a TE mode in an elliptical waveguide are shown, as an example, in Figs. 2–4, respectively.

IV. CONCLUSION

In this paper, a unified representation of the wave modes inside a hollow conducting waveguide of a series of cross sections is made by the use of the Rayleigh–Ritz method and the electromagnetic wave propagation characteristics in the waveguides are analyzed. Being of practical applications, these waveguide cross sections can be expressed in a unified manner by using the superquadric functional representation. As examples of application of the developed theory, various practically useful geometries including rectangular, circular, elliptical, coaxial, triangular, and general superquadric cross sections have been studied in a unified way. In the analysis, both TE and TM waves have

been considered and characterized. The calculated results in this paper have been compared with those analytical results available in the literature and an excellent agreement has been found. Certainly, some new results have also been produced so as to gain more physical insight into the wave modes. This method presented in the paper has been shown to be stable, efficient, and especially useful to analyze the wave modes or fields in waveguides of complicated cross-sectional geometries where the exact results are impossible and/or analytical/numerical methods are difficult to use or very time consuming.

REFERENCES

[1] N. Marcuvitz, *Waveguide Handbook*. Stevenage, U.K.: Peregrinus, 1986.

[2] S. Ramo, J. R. Whinnery, and T. V. Duzer, *Fields and Waves in Communication Electronics*. New York: Wiley, 1965.

[3] J. B. Davies and J. G. Kretzschmar, "Analysis of hollow elliptical waveguides by polygon approximation," *Proc. Inst. Elect. Eng.*, vol. 119, pp. 519–522, 1972.

[4] B. K. Wang, K. Y. Lam, M. S. Leong, and P. S. Kooi, "A new set of orthogonal polynomial functions for waveguide analysis," *Microwave Opt. Technol. Lett.*, vol. 7, no. 1, pp. 12–14, Jan. 1994.

[5] ——, "Elliptical waveguide analysis using improved polynomial approximation," *Proc. Inst. Elect. Eng.*, vol. 141, no. 6, pp. 483–488, Dec. 1994.

[6] M. A. Jensen and Y. Rahmat-Samii, "Electromagnetic characteristics of superquadric wire loop antennas," *IEEE Trans. Antennas Propagat.*, vol. 42, pp. 264–269, Feb. 1994.

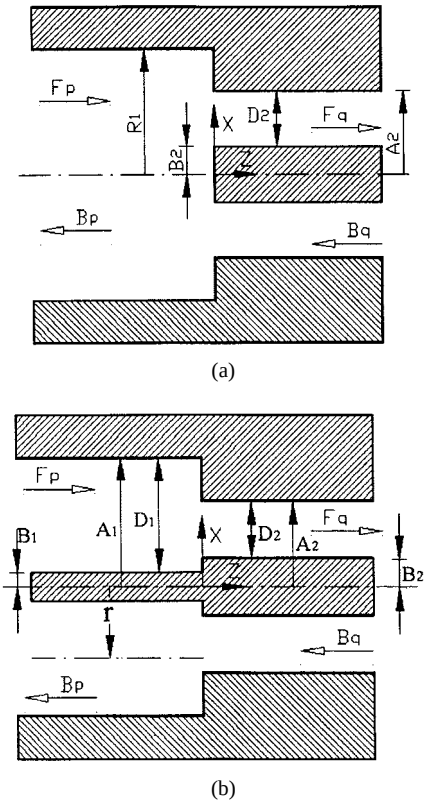

Fig. 1. Circular and coaxial waveguide step discontinuities. (a) A circular to a smaller coaxial waveguide step discontinuity (aperture area S_α: $b_2 \le \rho \le a_2$). (b) A coaxial waveguide step discontinuity (aperture area S_α: $b_2 \le \rho \le a_2$).

A Mode-Matching Technique for the Study of Circular and Coaxial Waveguide Discontinuities Based on Closed-Form Coupling Integrals

Anastasios P. Orfanidis, George A. Kyriacou, and John N. Sahalos

***Abstract*—A mode-matching scheme for the analysis of concentric circular and/or coaxial waveguide step discontinuities is proposed in this paper. An analytical evaluation of the involved coupling integrals for all possible discontinuities formed by any combination of a circular and a coaxial waveguide is performed. The originality mainly concerns the multimode excitation and scattering at a circular-to-coaxial waveguide step junction. Numerical results for a number of applications are compared against those of other techniques and/or measurements and are found to be in good agreement.**

***Index Terms*—Analytical evaluation of coupling integrals, circular–coaxial waveguide discontinuities, coaxial iris, mode-matching technique.**

I. INTRODUCTION

Circular or coaxial waveguide discontinuities have received significant attention (e.g., [1]) and approximate equivalent circuits have been given. Recent literature have put a new effort toward the study of coaxial discontinuities and irises in waveguides [2], [3], mostly using a classical mode-matching approach. It is also important to point out that there is lack of published data for irises in circular and coaxial waveguides [3], which are important in a variety of applications, and especially in the waveguide filters. A disadvantage of the analyses given in the past (e.g., [1]) is their approximate nature and the fact that they treat only isolated discontinuities. Both of them can be overcome when the whole structure is analyzed using a mode-matching technique provided that this is made fast enough as required by synthesis algorithms. The present effort is exactly directed toward this aim. For this purpose, the circular-to-coaxial and coaxial-to-coaxial junctions excited by single or multiple modes are analytically studied. The coupling integrals involved in the mode matching are given in closed-form expressions in a manner similar to that of [4]. The scattering from the junction of two offset circular waveguides was first studied analytically by Knetsch [5], [6] and reconsidered again in [2], [7], and [8]. The corresponding expressions of the present method, except for concentric waveguides, are identical to those of [2], [5], and [7]. The junction of two coaxial waveguides, but only for a TE_{11} excitation, was studied analytically by James [3]. This paper is an extension of [2]–[4], as far as concentric discontinuities are concerned, since it includes the previous cases, but for multimode excitation, and it additionally covers the circular-to-coaxial junction. To the authors' knowledge, mode-matching analytical results for the latter case are presented for the first time. Moreover, this case enables the analysis of coaxial irises in circular waveguides.

Manuscript received December 16, 1999.

A. P. Orfanidis and G. A. Kyriacou are with the Department of Electrical and Computer Engineering, Demokritos University of Thrace, GR-67100 Xanthi, Greece.

J. N. Sahalos is with the Department of Physics, Aristotle University of Thessaloniki, GR 540 06 Thessaloniki, Greece.

Publisher Item Identifier S 0018-9480(00)03761-3.

II. FORMULATION

A junction of two circular or two coaxial waveguides with different cross section, as well as a junction between a circular and coaxial wave-

guide, are considered. For each junction (see Fig. 1), a common axis of symmetry (axis-z) for the two waveguides with perfectly conducting walls is assumed. The electromagnetic field inside each waveguide is expanded into a modal series, e.g., Marcuvitz [1, p. 72]. Modes are numbered in an increasing sequence as they occur. Namely $p = 0, 1, 2, 3, \cdots$ denotes TEM, TE_{11}, TM_{01}, TE_{21}, etc. To have the field expressions independent of the magnitude of the excitation, a normalization of the mode functions to the mode propagating power (P_p) at the junction ($z = 0$) is made. The normalization coefficient N_p is defined as $N_p = 1/\sqrt{P_p}$ and it can be calculated from [1, pp. 67, 73, and 75] for the circular and coaxial waveguides. For the circular and the coaxial waveguides, the mode eigenvalues (χ_{mn}, χ'_{mn}) and (k_{mn}, k'_{mn}) are correspondingly given in [1, pp. 66–72]. A classical mode-matching technique has been employed, as described in [9], which finally gives the generalized scattering parameters that fully characterize the junction. Their expressions are [9, p. 16] as follows:

$$[\boldsymbol{S}_{11}]_{pq} = \Big([\boldsymbol{Q}]_{pq}[\boldsymbol{Q}]^T_{pq} + [\boldsymbol{I}]\Big)^{-1}\Big([\boldsymbol{Q}]_{pq}[\boldsymbol{Q}]^T_{pq} - [I]\Big)$$

and

$$[\boldsymbol{S}_{12}]_{pq} = 2\Big([\boldsymbol{Q}]_{pq}[\boldsymbol{Q}]^T_{pq} + [\boldsymbol{I}]\Big)^{-1}[\boldsymbol{Q}]_{pq}$$

$$[\boldsymbol{S}_{21}]_{pq} = [\boldsymbol{Q}]^T_{pq}\Big([\boldsymbol{I}] - [\boldsymbol{S}_{11}]_{pq}\Big)$$

and

$$[\boldsymbol{S}_{22}]_{pq} = [\boldsymbol{I}] - [\boldsymbol{Q}]^T_{pq}[\boldsymbol{S}_{12}]_{pq} \tag{1}$$

The elements of the $[\boldsymbol{Q}]$ matrix are known as coupling integrals and result from the application of the boundary conditions at the junction. These can be alternatively expressed from the electric $\overline{e}(\rho, \varphi)$ or the magnetic $\overline{h}(\rho, \varphi)$ modal functions

$$[Q_{pq}] = [Q^e_{pq}] = [Q^m_{pq}]^T \tag{2a}$$

with

$$\boldsymbol{Q}^e_{qj} = \frac{1}{2}(\boldsymbol{Y}_p)^{1/2}(\boldsymbol{Y}_q)^{-1/2}\iint\limits_{S_a}\overline{\boldsymbol{e}}^{\,\mathrm{II}}_q\cdot\overline{\boldsymbol{e}}^{\,\mathrm{I}}_j\,ds_2. \tag{2b}$$

$\boldsymbol{Y}_p$ is the pth-mode wave admittance and $\boldsymbol{S}_a$ is the common area of the two waveguides at the junction. Since modes can be either TEM, TE, or TM, the combinations (p, q) in (2) denote coupling between these modes. Integrals of (2) include Bessel functions with different orders and arguments and they require an increased computational effort, especially for microwave network synthesis applications. The transformation of cylindrical-to-rectangular coordinates ($\hat{x} = \hat{\rho}\cos\phi - \hat{\phi}\sin\phi$ and $\hat{y} = \hat{\rho}\sin\phi + \hat{\phi}\cos\phi$) reduces the coupling integrals into an expression known as the Lommel integral [4]. This integral can be evaluated analytically, e.g., Abramowitz and Stegun [10, p. 484]. For an integrand involving a product of Bessel functions $\mathcal{Z}_m$ and $\mathfrak{B}_m$ with the same order, we obtain

$$\begin{aligned}\mathfrak{F}_m(\mathcal{Z}_m, B_m, a) &= \int_0^a \mathcal{Z}_m(x_1\rho)\mathfrak{B}_m(x_2\rho)\rho\,d\rho\\ &= \frac{a}{x_1^2 - x_2^2}\Big\{x_1\mathcal{Z}_{m+1}(x_1a)\mathfrak{B}_m(x_2a)\\ &\qquad - x_2\mathcal{Z}_m(x_1a)\mathfrak{B}_{m+1}(x_2a)\Big\}\end{aligned} \tag{3}$$

where $\mathcal{Z}_m$ and $\mathfrak{B}_m$ denote any of the J_m and Y_m Bessel functions.

For the case of a nonzero lower limit in the integral, e.g., integrating from b to a, (3) is used twice and another function is introduced as

$$\mathfrak{S}_m(\mathcal{Z}_m, \mathfrak{B}_m) = \mathfrak{F}_m(\mathcal{Z}_m, \mathfrak{B}_m, a) - \mathfrak{F}_m(\mathcal{Z}_m, \mathfrak{B}_m, b). \tag{4}$$

The transformation of the modal functions from cylindrical-to-rectangular coordinates and their substitution in (2) is carried out. Employing the formulas of (3) and (4), we have the following.

• Coupling between two circular waveguides

$$Q_{pq} = Q_{mn,il} = \begin{cases} N^{\mathrm{TE}}_{c,p}N^{\mathrm{TE}}_{c,q}\sqrt{\dfrac{\gamma_p}{\gamma_q}}\,\dfrac{\chi'_{mn}\chi'_{il}}{R_1R_2}\{\Phi_m + 1 + \Phi_{m-1}\}, \\ \quad \mathrm{TE}\text{ - }\mathrm{TE} \\ -N^{\mathrm{TE}}_{c,p}N^{\mathrm{TM}}_{c,q}\,\dfrac{\sqrt{\gamma_p\gamma_q}}{k_0}\,\dfrac{\chi'_{mn}\chi_{il}}{R_1R_2}\{\Phi_{m+1} + \Phi_{m-1}\}, \\ \quad \mathrm{TE}\text{ - }\mathrm{TM} \\ 0, \qquad \mathrm{TM}\text{ - }\mathrm{TM} \\ N^{\mathrm{TM}}_{c,p}N^{\mathrm{TM}}_{c,q}\sqrt{\dfrac{\gamma_q}{\gamma_p}}\,\dfrac{\chi_{mn}\chi_{il}}{R_1R_2}\{\Phi_{m+1} + \Phi_{m-1}\}, \\ \quad \mathrm{TM}\text{ - }\mathrm{TM} \end{cases} \tag{5}$$

where

$$\Phi_k = \int_0^{R_2} J_k\left(\frac{\chi_{mn}}{R_1}\rho\right)\cdot J_k\left(\frac{\chi_{il}}{R_2}\rho\right)\rho\,d\rho = \mathfrak{F}_k(J_k, J_k, R_2).$$

• Coupling between a circular and smaller coaxial waveguide [see Fig. 1(a)]

$$Q_{pq} = Q_{mn,il} = \begin{cases} N^{\mathrm{TE}}_{c,p}N^{\mathrm{TE}}_{x,q}\sqrt{\dfrac{\gamma_p}{\gamma_q}}\,\dfrac{\chi'_{mn}\kappa'_{il}\pi}{4R_1} \\ \quad \cdot\Big\{Y'_m(\kappa'_{il}b)[X_{m+1} + X_{m-1}] \\ \qquad + J'_m(\kappa'_{il}b)[\Psi_{m+1} + \Psi_{m-1}]\Big\}, \qquad \text{for TE - TE} \\ -N^{\mathrm{TE}}_{c,p}N^{\mathrm{TM}}_{x,q}\,\dfrac{\sqrt{\gamma_p\gamma_q}}{k_0}\,\dfrac{\chi'_{mn}\kappa_{il}\pi}{4R_1} \\ \quad \cdot\Big\{Y_m(\kappa_{il}b)[X_{m-1} - X_{m+1}] \\ \qquad - J_m(\kappa_{il}b)[\Psi_{m+1} - \Psi_{m-1}]\Big\}, \qquad \text{for TE - TM} \\ 0, \qquad \text{for TM - TE} \\ -N^{\mathrm{TM}}_{c,p}N^{\mathrm{TM}}_{x,q}\sqrt{\dfrac{\gamma_q}{\gamma_p}}\,\dfrac{\chi_{mn}\kappa_{il}\pi}{4R_1} \\ \quad \cdot\Big\{Y_m(\kappa_{il}b)[X_{m-1} + X_{m+1}] \\ \qquad - J_m(\kappa_{il}b)[\Psi_{m+1} + \Psi_{m-1}]\Big\}, \qquad \text{for TM - TM} \\ -N^{\mathrm{TM}}_{c,p}N^{\mathrm{TEM}}_{x,q}\sqrt{\dfrac{\gamma_q}{\gamma_p}}\,\dfrac{\chi_{0n}\pi}{R_1}\Big[J_0(\kappa_{il}a) - J_0(\kappa_{il}b)\Big]\Big/\kappa_{il}, \\ \quad \text{for TM - TEM} \end{cases} \tag{6}$$

where

$$X_k = \int_b^a J_k\left(\frac{\chi_{mn}}{R_1}\rho\right)J_k(\kappa_{il}\rho)\rho\,d\rho = \mathfrak{S}_k(J_k, J_k, a, b),$$

$$\Psi_k = \int_b^a J_k\left(\frac{\chi_{mn}}{R_1}\rho\right)Y_k(\kappa_{il}\rho)\rho\,d\rho = \mathfrak{S}_k(J_k, Y_k, a, b).$$

• Coupling between a coaxial and a smaller circular waveguide: matrices Q_{pq} are the same as for the previous case interchanging p and q as well as χ_{mn} and κ_{il}.

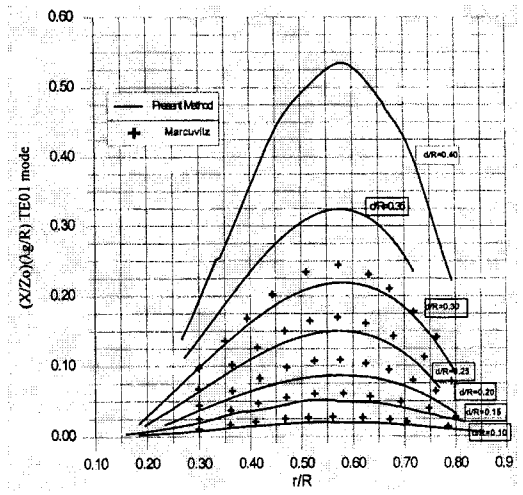

(a)

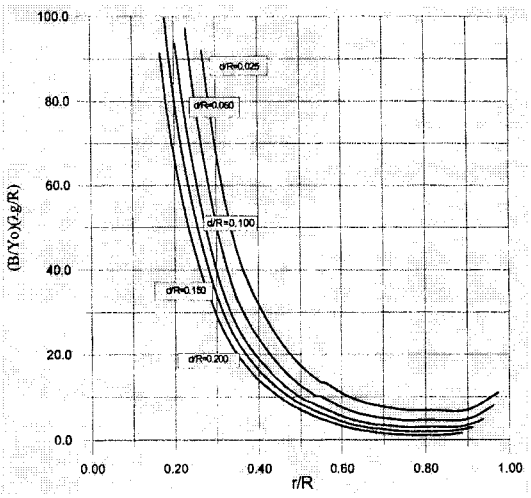

(b)

Fig. 2. Small coaxial iris introduced in a circular waveguide. (a) Normalized shunt inductance for a TE_{01} excitation. (b) Normalized shunt susceptance for a TM_{01} excitation.

• Coupling between two coaxial waveguides [see Fig. 1(b)]

$$Q_{pq} = Q_{mn,il} = \begin{cases} P_p^{\mathrm{TE}} P_q^{\mathrm{TE}} \sqrt{\gamma_p/\gamma_q}\, \kappa'_{mn} \kappa'_{il} \{\Xi_+ - \Delta_+\}/4, \\ \quad \text{for TE - TE} \\ N_{x,p}^{\mathrm{TE}} N_{x,q}^{\mathrm{TM}} \sqrt{\gamma_p \gamma_q}\, \kappa'_{mn} \kappa_{il}\, \pi \{\Xi_- + \Delta_-\}/(4k_0), \\ \quad \text{for TE - TM} \\ 0, \qquad \text{for TM - TE} \\ N_{x,p}^{\mathrm{TM}} N_{x,q}^{\mathrm{TM}} \sqrt{\gamma_q/\gamma_p}\, \kappa_{mn} \kappa_{il}\, \pi \{\Xi_+ - \Delta_+\}/R_1, \\ \quad \text{for TM - TM} \\ N_{x,p}^{\mathrm{TM}} N_{x,q}^{\mathrm{TEM}} \sqrt{\gamma_p/k_0}\, \kappa_{0n}\, \pi Y_0(\kappa_{mn} b_1) \\ \quad \cdot \Big[J_0(\kappa_{mn} b_1) - J_0(\kappa_{mn} b_1) \Big] \Big/ \kappa_{mn}, \qquad \text{for TM - TEM} \\ N_{x,p}^{\mathrm{TEM}} N_{x,q}^{\mathrm{TM}} \sqrt{k_0/\gamma_q}\, \kappa_{0l}\, \pi Y_0(\kappa_{il} b_2) \\ \quad \cdot \Big[J_0(\kappa_{il} b_2) - J_0(\kappa_{il} b_2) \Big] \Big/ \kappa_{il}, \qquad \text{for TEM - TM} \\ \ln(a/b) / \sqrt{\ln(a_1/b_1)\, \ln(a_2/b_2)}, \qquad \text{for TEM - TEM} \end{cases} \tag{7}$$

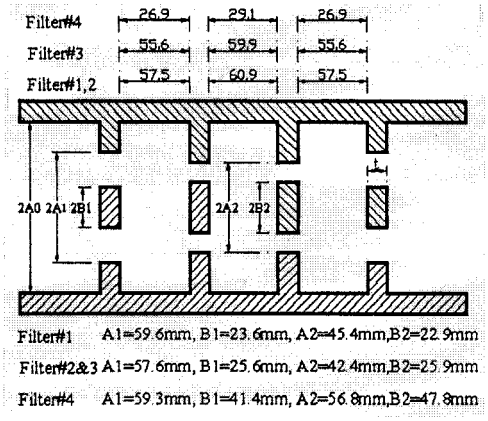

(a)

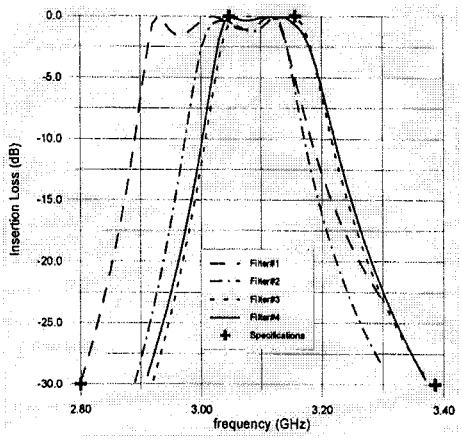

(b)

Fig. 3. TE_{01}-mode bandpass filter. (a) Geometry. (b) Frequency response (for $A_0 = 90$ mm and $t = 1$ mm).

where

$$\Omega_m(\mathcal{Z}_m, \mathfrak{B}_m) = \mathcal{Z}_m(k_{mn} b_1) \mathfrak{B}_m(k_{il} b_2)$$

$$\Xi_{k\pm} = \Omega_k(Y'_k, Y'_k) \mathfrak{S}\Big[J_{k\pm1}(\kappa_{mn}\rho), J_{k\pm1}(\kappa_{il}\rho) \Big] + \Omega_k(J'_k, J'_k) \mathfrak{S}\Big[Y_{k+1}(\kappa_{mn}\rho), Y_{k+1}(\kappa_{il}\rho) \Big]$$

$$\Delta_{k\pm} = \pm\, \Omega_k(Y'_k, J'_k) \mathfrak{S}\Big[J_{k\pm1}(\kappa_{mn}\rho), Y_{k\pm1}(\kappa_{il}\rho) \Big] \pm\, \Omega_k(J'_k, Y'_k) \mathfrak{S}\Big[Y_{k\pm1}(\kappa_{mn}\rho), J_{k\pm1}(\kappa_{il}\rho) \Big].$$

In the above expressions, each waveguide section can be assumed to be homogeneously filled with an isotropic dielectric or magnetic material, where the characteristics of the material are introduced through the wave admittance and propagation factor. For the TE_{11} excitation, (5) and (7) are exactly reduced to those of Wu [7, p. 277] and James [3], respectively. Equation (5) is also identical to that of Knetsch [5] for the concentric case.

III. Numerical Results and Discussions

Our formulation is first verified numerically for circular waveguide discontinuities. The analysis of a thick circular iris gave identical results to a moment-method solution [11] with a maximum deviation from measurements less than 1%. Nondominant mode excitations were also checked. For example, the analysis of a TE_{01} excited filter has

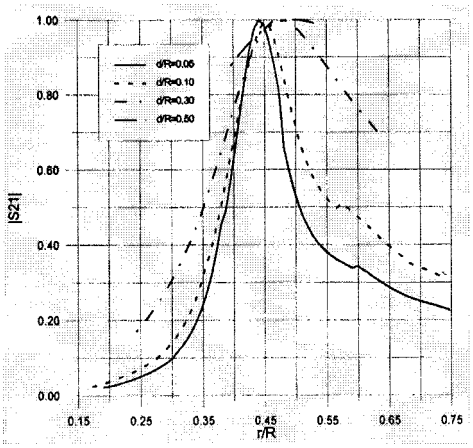

Fig. 4. Transmission coefficient for a thin coaxial iris introduced in a circular waveguide ($R = 12.7$ mm, $\lambda = 33$ mm) with a TE_{11} excitation.

shown an excellent agreement with [12]. Our first example presents a relatively thin coaxial iris ($t = 1$ mm thickness) introduced in a circular waveguide with a radius $a = 12.7$ mm and a TE_{01} excitation. The reflection coefficient (S_{11}) is evaluated as a function of the iris normalized aperture d/R and its normalized position (r/R). This iris can be described by an equivalent shunt inductance (jX) according to Marcuvitz [1, p. 247]. The corresponding results for jX are calculated from S_{11} and are shown in Fig. 2(a). A relatively good agreement between the present method and the data given by Marcuvitz [1, p. 249] is observed. This is justified by the fact that the iris analyzed here is an isolated as well as a thin one, just as considered in [1]. A similar investigation has been carried out for TM_{01} excitation. In this case, the iris can be described by an equivalent shunt susceptance shown in Fig. 2(b). The corresponding results for jB are calculated from S_{11}. Finally, a thick iris ($t = 5$ mm) excited by a TE_{01} mode has been analyzed and compared with the Hewlett-Packard Company software HFSS.[1] The results are found to be almost identical.

To show the improvement resulting from the employment of the present method in microwave circuit design, the bandpass filter example given in [13, p. 457] has been adapted to circular waveguides with coaxial irises [see Fig. 3(a)], which is either empty or filled with a dielectric material (RT/duroid $\varepsilon_r = 2.94$). Similar structures are also analyzed in [14], but using a different mode-matching approach, which is not based on closed-form expressions for the coupling integrals. The topology of this filter involves shunt inductances alternated with transmission-line sections (acting as impedance inverters). The specifications of the filter are shown in Fig. 3(b) with cross marks. For the first filter, the irises are estimated from the data given by Marcuvitz [1, p. 247], while for the second one, data taken by the present method [see Fig. 2(a)] are used. The response of these filters (#1 and #2) is shown in Fig. 3(b). A lower central frequency (f_{ce}) and a wider bandwidth (BW) are obtained from Marcuvitz data. This is mainly due to inaccuracy of the jX data [see Fig. 2(a)], which means that the desired jX value leads to a lower r/R in Fig. 2. In turn, the estimated r/R is introduced in the mode-matching method (for a more accurate simulation), which accounts for a lower jX value than the desired one. Thus, since the filter quality factor is proportional to $Q = f_{\mathrm{ce}}/\mathrm{BW} \propto X/R$, where R represents the ohmic losses, then the lower jX value will cause lower f_{ce} and wider BW. Furthermore, both designs present a significant passband VSWR ripple. A quasi-Newton optimization technique has been employed, allowing only for the transmission lines to be varied. An almost flat response in the passband is then obtained [Fig. 3(b), filter #3]. This procedure is then repeated for the dielectric filled waveguide (so that the irises are supported by the dielectric) to give filter #4, as shown in Fig. 3. A thin coaxial iris has also been analyzed for a TE_{11} excitation. This case presents resonance phenomena as shown in Fig. 4, where the magnitude of the transmission coefficient $|S_{21}|$ is plotted against the iris mid position (r/R) with its width (d/R) as a parameter. The resonance occurs around the mid-radius of the circular waveguide (r/R from 0.44 to 0.52) depending on the iris width.

[1]High-Frequency Structure Simulator (HFSS), Hewlett-Packard Company, Santa Rosa, CA, 1990.

IV. Conclusions

The step junction of concentric circular and/or coaxial waveguide is analytically studied using a mode-matching technique. The originality of the method mainly concerns themultimode excitation and the scattering at the circular-to-coaxial step discontinuity. The coupling integrals involved are first expressed as Lommel integrals and are then given in closed form. The resulted expressions can be included in microwave computer-aided design (CAD) software to improve its speed. Moreover, the present method could be extended to include the corresponding offset junction.

References

[1] N. Marcuvitz, *Waveguide Handbook*. Stevenage, U.K.: Peregrinus, 1986.
[2] Z. Shen and R. H. MacPhie, "Scattering by a thick off-centered iris in a circular waveguide," *IEEE Trans. Microwave Theory Tech.*, vol. 43, pp. 2639–2642, Nov. 1995.
[3] G. L. James, "Admittance of irises in coaxial and circular waveguides for TE_{11} mode excitation," *IEEE Trans. Microwave Theory Tech.*, vol. MTT-35, pp. 430–434, Apr. 1987.
[4] J. D. Wade and R. H. MacPhie, "Scattering at circular to rectangular waveguide junction," *IEEE Trans. Microwave Theory Tech.*, vol. MTT-34, pp. 1085–1091, Nov. 1986.
[5] H. D. Knetsch, "Axial offsets of circular waveguides of arbitrary radii" (in German), *Arch. Elektron. Uebertrag.*, vol. 23, pp. 23–32, Jan. 1969.
[6] ——, "Theory of circular waveguide discontinuities" (in German), *Arch. Elektron. Uebertrag.*, vol. 22, pp. 591–600, 1968.
[7] C. P. Wu, "Variational and iterative methods for waveguides and arrays," in *Computer Techniques for Electromagnetics*, 2nd ed, R. Mittra, Ed. New York: Summa Books, 1987.
[8] E. Kuhn and V. Hombach, "Computer-aided analysis of corrugated horns with axial or ring loaded radial slots," in *Proc. ICAP'88*, pp. 127–131.
[9] J. Uher, J. Bornemann, and U. Rosenberg, *Waveguide Components for Antenna Feed Systems: Theory and CAD*. Norwood, MA: Artech House, 1993.
[10] M. Abramowitz and I. A. Stegun, *Handbook of Mathematical Functions*. New York: Dover, 1965.
[11] R. W. Sharstein and A. T. Adams, "Thick circular iris in a TE_{11} mode circular waveguide," *IEEE Trans. Microwave Theory Tech.*, vol. 36, pp. 1529–1531, Nov. 1988.
[12] U. Papziner and F. Arndt, "Field theoretical computer aided design of rectangular and circular iris coupled rectangular or circular waveguide cavity filters," *IEEE Trans. Microwave Theory Tech.*, vol. 41, pp. 462–471, Mar. 1993.
[13] G. L. Matthaei, L. Young, and E. M. T. Jones, *Microwave Filters, Impedance-Matching Networks, and Coupling Structures*. New York: McGraw-Hill, 1964.
[14] C. Wang, A. Zaki, and A. E. Atia, "Dual-mode conductor loaded cavity filters," *IEEE Trans. Microwave Theory Tech.*, vol. 45, pp. 1240–6, Aug. 1997.